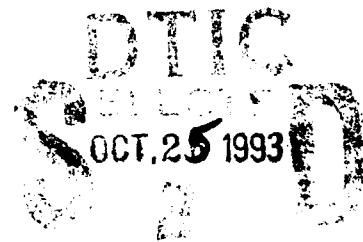AD-A270 857

|||||||||||||||||||||||

NAVAL POSTGRADUATE SCHOOL
Monterey, California

DISSERTATION

A STUDY OF THE AMPLIFICATION OF LASER AND VLF WAVES
USING A SIMPLE PENDULUM MODEL

by

Keith Alan Sturgess

June 1993

Dissertation Advisor: William B. Colson

Approved for public release; distribution is unlimited.

93-25415

|||||||||||||||||||||||

93 10 21 000

REPORT DOCUMENTATION PAGE

Public reporting burden for this collection of information is estimated to average 1 hour per response, including the time for reviewing instructions, searching existing data sources, gathering and maintaining the data needed, and completing and reviewing the collection of information. Send comments regarding this burden estimate or any other aspect of this collection of information, including suggestions for reducing this burden to Washington Headquarters Services, Directorate for Information Operations and Reports, 1215 Jefferson Davis Highway, Suite 1204, Arlington, VA 22202-4302, and to the Office of Management and Budget, Paperwork Reduction Project (0704-0188), Washington, DC 20503

1. AGENCY USE ONLY (Leave blank)	2. REPORT DATE June 1993	3. REPORT TYPE AND DATES COVERED Dissertation

4. TITLE AND SUBTITLE A Study of the Amplification of Laser and VLF Waves Using a Simple Pendulum Model	5. FUNDING NUMBERS
6. AUTHOR(S) Keith Alan Sturgess	

7. PERFORMING ORGANIZATION NAME(S) AND ADDRESS(ES) Naval Postgraduate School Department of Physics Monterey, California 93943	8. PERFORMING ORGANIZATION REPORT NUMBER

9. SPONSORING/MONITORING AGENCY NAME(S) AND ADDRESS(ES)	10. SPONSORING/MONITORING AGENCY REPORT NUMBER

11. SUPPLEMENTARY NOTES

12a. DISTRIBUTION/AVAILABILITY STATEMENT Approved for Public Release; distribution is unlimited.	12b. DISTRIBUTION CODE

13. ABSTRACT (Maximum 200 words) The Lorentz force equation governing the interaction between radiation and charged particles in the presence of a static magnetic field can be reduced to the form of the simple pendulum equation, when applied to the Free Electron Laser (FEL) and to the amplification of whistler waves in the magnetosphere.

The first topic in this thesis is the start-up of an FEL with a compact design having a small, spatial undulator period, many periods, and a small undulator field strength. Under these conditions, the number of photons spontaneously emitted into the resonator mode each pass is so small that a classical field cannot be established. Quantum fluctuations affect the wave-particle interaction and therefore diminish weak field gain. An FEL start-up condition, several orders of magnitude more restrictive than determined by quantum recoil alone, is derived from the photon rate equation.

The next topic is the evolution of a weak, classical radiation field driven by a long electron pulse. Assuming low gain, it is

14. SUBJECT TERMS Free Electron Laser, FEL, undulator, start-up, quantum fluctuations, longitudinal modes, whistler waves, pendulum equation, numerical simulation.	15. NUMBER OF PAGES 103
	16. PRICE CODE

17. SECURITY CLASSIFICATION OF REPORT UNCLASSIFIED	18. SECURITY CLASSIFICATION OF THIS PAGE UNCLASSIFIED	19. SECURITY CLASSIFICATION OF ABSTRACT UNCLASSIFIED	20. LIMITATION OF ABSTRACT UL

NSN 7540-01-280-5500

13. Continued

possible to reduce the coupled optical wave and electron pendulum equation to a simple, first-order, partial differential equation including electron dynamics, slippage, desynchronism, and resonator losses. This analytical method is used to study coherence development, and the effects of varying the electron beam pulse shape.

Next, the Boeing Average Power Laser Experiment (APLE) is investigated using two and three dimensional numerical simulations. Various methods of reducing the electron-radiation coupling in the oscillator are examined in order to minimize the electron beam energy spread introduced into the FEL amplifier. An alternative for achieving high power makes use of the oscillator alone, but with a tapered undulator to increase the electron-radiation coupling.

The final topic is charges particles, following helical trajectories, traveling in the magnetosphere between mirror points along the earth's magnetic field lines. When electrons interact with a whistler wave near the geomagnetic equator, their motion can again be described by the simple pendulum equation. The inhomogeneity of the earth's magnetic field near the geomagnetic equator is analogous to the field in a tapered undulator. Numerical phase-space simulations are developed to investigate the interaction.

A Study of the Amplification of Laser and VLF Waves Using a Simple Pendulum Model

by

Keith Alan Sturgess

Captain, United States Army
B.S., Florida Institute of Technology, 1983

Submitted in partial fulfillment of the
requirements for the degree of

DOCTOR OF PHILOSOPHY IN PHYSICS
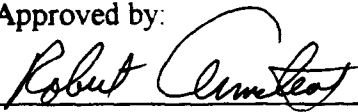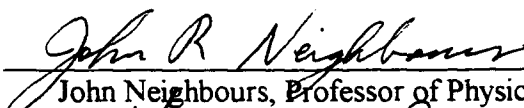
from the

NAVAL POSTGRADUATE SCHOOL

June, 1993

Author: _____
Keith A. Sturgess

Approved by:

_____   _____
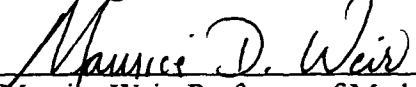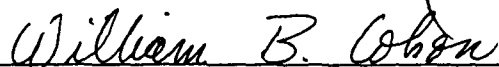Robert Armstead, Professor of Physics   John Neighbours, Professor of Physics
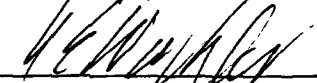
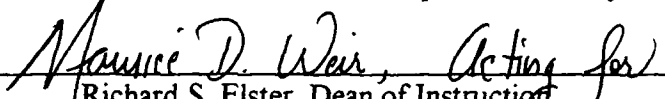_____   _____
Rudolf Panholzer, Professor of Space Science   Maurice Weir, Professor of Mathematics

_____
William B. Colson, Dissertation Advisor

_____
Karlheinz E. Woehler, Chairman, Department of Physics

_____
Richard S. Elster, Dean of Instruction

ABSTRACT

The Lorentz force equation governing the interaction between radiation and charged particles in the presence of a static magnetic field can be reduced to the form of the simple pendulum equation, when applied to the Free Electron Laser (FEL) and to the amplification of whistler waves in the magnetosphere.

The first topic in this thesis is the start-up of an FEL with a compact design having a small, spatial undulator period, many periods, and a small undulator field strength. Under these conditions, the number of photons spontaneously emitted into the resonator mode each pass is so small that a classical field cannot be established. Quantum fluctuations affect the wave-particle interaction and therefore diminish weak-field gain. An FEL start-up condition, several orders of magnitude more restrictive than determined by quantum recoil alone, is derived from the photon rate equation.

The next topic is the evolution of a weak, classical radiation field driven by a long electron pulse. Assuming low gain, it is possible to reduce the coupled optical wave and electron pendulum equation to a simple, first-order, partial differential equation including electron dynamics, slippage, desynchronism, and resonator loss. This analytical method is used to study coherence development, and the effects of varying the electron beam pulse shape.

Next, the Boeing Average Power Laser Experiment (APLE) is investigated using two and three dimensional numerical simulations. Various methods of reducing the electron-radiation coupling in the oscillator are examined in order to minimize the electron beam energy spread introduced into the FEL amplifier. An alternative for achieving high power makes use of the oscillator alone, but with a tapered undulator to increase the electron-radiation coupling.

The final topic is charged particles, following helical trajectories, traveling in the magnetosphere between mirror points along the earth's magnetic field lines. When electrons interact with a whistler wave near the geomagnetic equator, their motion can again be described by the simple pendulum equation. The inhomogeneity of the earth's magnetic field near the geomagnetic equator is analogous to the field in a tapered undulator. Numerical phase-space simulations are developed to investigate the interaction.

Table of Contents

ACKNOWLEDGEMENT

As with any significant effort, there are many people directly and indirectly responsible for the success of this dissertation. I would like to first thank Bill Colson, who took me in, gave me interesting projects to work on, and stood behind me and pushed when the going got tough down the home stretch. Second, my thanks go out to Professors Armstead and Neighbours who gave valuable input into the writing of this dissertation, and whose assistance in preparing for the oral exams was essential.

There is no way to quantify all of the help my wife, Lynn, has been to me during the writing of this dissertation. She was my second reader for spelling and grammar. She made all of the changes for a rewrite while I was away on TDY in Kansas and Virginia. She accompanied me on several research and conference trips and probably knows more about free electron lasers than some physicists. Her love and understanding were a constant source of unwavering support that helped me get through some difficult days and weeks. I only hope I support her as well as she did me when she is working toward her doctorate.

I. INTRODUCTION

A free electron laser (FEL) oscillator uses a beam of relativistic electrons passing through a periodic undulator to produce and amplify light stored within a resonator. Since this light is a product of the electron - undulator interaction, its properties (i.e. wavelength and power) can be changed by altering the properties of the electron beam and the undulator. The ease of tunability of the FEL over a wide range of wavelengths is beginning to make the FEL a sought after piece of equipment by many disciplines in universities, research labs, and industry. The promise of high efficiency and high average power has made the FEL a research priority of the armed forces as they seek a speed-of-light weapon.

The basic physics of an FEL is presented in Chapter II as a starting point for the research chapters that follow. The FEL theory presented here uses Maxwells' field equations to describe the evolution of the light in response to the bunching electrons, and self-consistently uses the pendulum equation to describe the evolution of the bunching electrons in response to the light [1].

Chapter III examines FEL physics during the first several passes of the electrons through a compact undulator that uses many short periods and a small undulator parameter. Spontaneous emission is introduced, and the effects of a small number of photons in the resonator causes statistical fluctuations of the photon number. These quantum fluctuations, if large enough, can significantly degrade the classical, small-signal gain of the FEL causing slow start-up or possibly the failure of the FEL to start.

New and original research concerning the problem of quantum limitations on the start-up of FELs is presented in Chapter III. The previously derived equation for gain including photon fluctuations is incorporated into the photon rate

equation to obtain a new start-up condition. The photon rate equation is then solved analytically using the new expression for gain. This and other analytical results are compared with those obtained by other authors using a completely quantum mechanical method. Also, the new expression for gain is incorporated into a numerical simulation to solve for optical mode evolution.

Chapter IV follows the evolution of long optical pulses using a partial-differential equation which includes effects of desynchronism and resonator losses. Desynchronism describes the misalignment between the optical and electron pulses on successive passes through the resonator. Analytical expressions are derived for the optical wave evolution assuming a long electron pulse, while the FEL operates in the small signal, low gain regime. The first-order, partial-differential equation is then used to examine the effects of the electron pulse shape on the final optical pulse. Also, the coherence development from a random incoherent optical pulse to a final coherent optical pulse is examined.

A partial-differential equation describing optical pulse evolution is used for new and original research in Chapter IV. The single-pass, first-order partial-differential equation is extended from one to multiple passes including desynchronism and resonator losses. The partial-differential equation is solved analytically for the case of a continuous electron beam, a parabolic electron pulse shape, and a Gaussian electron pulse. A desynchronism curve showing the variation of optical power with desynchronism is then created from the analytical solution for a parabolic electron pulse shape and compared to desynchronism curves produced numerically, experimentally, and with analytical methods used by other authors. It is shown that exact synchronism gives zero optical power in steady-state. The case of a triangular electron pulse is solved analytically. A numerical FEL simulation is modified to solve the single-pass

2

partial-differential equation and used to study coherence evolution. Finally, a numerical code is developed to compare the analytical solution and the numerical FEL simulation for the cases of a parabolic, triangular or continuous electron pulse.

Only weak optical fields are studied through Chapter IV. Chapter V examines the Boeing/LANL high Average Power Laser Experiment (APLE). Since the proposed design of APLE has a single electron beam powering both an oscillator and amplifier FEL in series, it is important that the oscillator FEL not induce a large energy spread in the electron beam prior to the amplifier FEL. Chapter V examines methods of reducing the electron - light coupling in the oscillator. One method of reducing the coupling calls for inducing a ramp, or a slew, in energy along the electron pulse. Running the oscillator alone as a high average power FEL is also examined.

The investigation into methods of reducing the electron beam energy spread induced by the FEL oscillator at the Boeing APLE project is new and original research. A numerical FEL simulation is extended to accurately calculate the optical field evolution in the presence of large desynchronism. Using this modification, a desynchronism curve is presented for the APLE oscillator. The desynchronism that best reduces the electron energy spread for the APLE oscillator is found. The simulation is modified further to include the effects of energy and timing jitter of the electron pulse from the accelerator. These effects are explored for large and small values of desynchronism. The simulation is modified again to include an energy slew across the electron micropulse in order to show that the energy spread induced in the electron beam is more than Boeing researchers had expected. The final APLE topic explores the tapered oscillator design as a high average power device. Conditions are obtained for achieving the optimum power from the FEL oscillator alone with no amplifier.

Finally, Chapter VI examines whistler wave amplification employing the similar theoretical and simulation methods used to understand the FEL. The whistler and FEL both have electrons in helical trajectories coupling to and amplifying a transverse electromagnetic wave. The wave and electron equations of motion are developed for the whistler interaction including the inhomogeneity due to the variation in magnetic field strength along a field line of the earth's magnetic field. Simulations are then developed from these equations in order to describe stimulated VLF emission.

Chapter IV includes new and original research on whistler wave amplification using a wave equation driven by the pendulum equation. As a member of a team, I participated in the derivation of the homogeneous and inhomogeneous wave equation and electron equations of motion. Next, the team developed numerical simulations of VLF wave amplification. Using the numerical simulations, the effects of homogeneous and inhomogeneous magnetic fields are explored, as well as the effects of a spread in phase velocity. The phase- space evolution of the electrons and the growth of the optical pulse power and phase are displayed graphically in order to better understand their coupled dynamics.

Much of the research in this thesis has been presented at scientific conferences, published, or submitted for publication. The research in Chapter III will be submitted to Physical Review Letters under the title "A Quantum Limitation on the Start-up of Compact Free Electron Lasers" by K. A. Sturgess and W. B. Colson. The research in Chapter IV was presented at the Thirteenth International Free Electron Laser Conference in Sante Fe, New Mexico (August 1991), and resulted in the publication of a paper titled "An Analytical Solution to Longitudinal Modes in Free Electron Lasers" by K. A. Sturgess and W. B. Colson in *Nuclear Instruments and Methods in Physics Research*, **A318,** pages

576-581, (1992). The research in Chapter V was presented at the Fourteenth International Free Electron Laser Conference in Kobe, Japan. (August 1992) and accepted for publication in *Nuclear Instruments and Methods in Physics Research* with the title "Short Pulse Evolution in the Boeing/LANL APLE Oscillator" by K. Sturgess, D. J. Frost and W. B. Colson. The research in Chapter VI was presented at the Fourteenth International Free Electron Laser Conference in Kobe, Japan, (August 1992), and accepted for publication in *Nuclear Instruments and Methods in Physics Research* with the title "Analogies Between the Free Electron Laser and Whistler Wave Amplification in the Magnetosphere" by W. B. Colson, B. Gately, D. L. Caudle, and K. Sturgess.

II. FREE ELECTRON LASER THEORY

A. INTRODUCTION

An operating Free Electron Laser (FEL) consists of an accelerator capable of driving electrons to relativistic energies, an undulator composed of a transverse, periodic magnetic field that "wiggles" the electrons, and optical devices necessary to collect and transport the amplified radiation. The periodically deflected relativistic electrons radiate spontaneously, and in addition, couple to the radiation store in an optical resonator leading to coherent stimulated emission. The idea of an FEL was conceptually introduced in 1971 by J.M.J. Madey [2]. Related work which contributed to the FEL include the traveling wave tube of Motz [3], and the ubitron developed by Philips [4]. Successful experimental operation of the FEL amplifier in 1976 [5] and an FEL oscillator in 1977 [6] demonstrated the feasibility and potential of this new laser device.

As mentioned above, the undulator's role in an FEL is to give the relativistic electrons periodic transverse deflections as they travel with the light pulse down the length of the undulator. This deflection, provided by either permanent magnets or electromagnets, allows the electrons to couple to, and transfer energy with the transverse optical pulse along the undulator length, $L = N\lambda_0$ where λ_0 is the undulator wavelength and N is the number of periods in the undulator. An important dimensionless quantity characterizing the undulator is the undulator parameter $K = e\bar{B}\lambda_0/2\pi mc^2$, where $\bar{B}$ is the rms field strength over one period of the undulator, e is the electron charge magnitude, m is the mass of the electron, and c is the speed of light. In most FEL's, $K \approx 0.1 \rightarrow 5$.

6

There are two main types of undulator, based on the paths electrons take within them: helical and linearly polarized. A helical undulator produces helical electron paths, which produces and couples to circularly-polarized light. The ideal helical magnetic field is constant in magnitude along the longitudinal axis of the undulator, and in rectangular coordinates is given by [1]

$$\bar{B}_H = B[cos(k_0 z), sin(k_0 z), 0]. \tag{2-1}$$

where B is the peak magnetic field strength on this axis, and $k_0 = 2\pi/\lambda_0$ is the undulator wave number. The helical undulator design focuses electrons toward the undulator axis, since the average magnetic field can be expanded and shown to increase off-axis as

$$\bar{B} = B\left(1 + \frac{k_0^2 r^2}{4} + ...\right), \tag{2-2}$$

where r is the distal distance from the axis of the undulator.

A linearly-polarized undulator produces periodic planar motion in the electron beam which in turn produces and couples to linearly-polarized light. The linear magnetic field has an rms field strength of $B/\sqrt{2}$ which is less than the helical case, and so, couples less well to the light and produces half the gain. In rectangular coordinates, the linear field is given by

$$\bar{B}_L = B[0, sin(k_0 z), 0] \tag{2-3}$$

and provides magnetic focusing in one direction only.

The accelerators used in various FEL projects range from low energy Van De Graff electrostatic accelerators to high energy storage rings, including intermediate energy microtrons and linear accelerators. They span an energy range giving Lorentz factors $\gamma \approx 10 \rightarrow 10^3$, where $\gamma^{-1} = \sqrt{1 - v^2/c^2}$, and

7

electron beam currents ranging from $I \approx 1 \rightarrow 10^3 A$. The typical RF linac produces electron micropulses of length, $l_e \approx mm \rightarrow cm$, separated by about one to several meters grouped together in a long macropulse of $1 \mu s$ to $1 ms$. Th transverse radius of the electron beam is on the order of millimeters resulting in an electron density of $\rho \approx 10^{12} \rightarrow 10^{13} cm^{-3}$.

The electron beam quality is characterized by its energy spread and emittance. Energy spread describes the spread of electron velocities in the beam and is characterized by $\Delta\gamma/\gamma$. Emittance is defined as $\varepsilon \approx \bar{r}_0\bar{\theta}_0$, where $\bar{r}_0$ is the rms initial position spread of the electrons in the beam, and $\bar{\theta}_0$ is the rms initial angular spread in the beam. Although the angular and position spread of the beam can be varied, the emittance of the beam tends to be a constant for an accelerator at a given energy. Normalized emittance, $\varepsilon_n \approx \gamma\varepsilon$, tends to be constant along the accelerator while the electrons are increasing their energies.

When the electron beam enters the undulator, it is desirable to choose the angular and position spreads in the beam so that it does not excessively focus or expand as it travels down the length of the undulator. For a fixed value of emittance, a small beam radius at one point along the undulator results in a large angular spread, and consequently a large beam radius farther along the undulator. A small angular spread results in a large beam radius everywhere. The condition that minimizes the beam radius along the undulator is called the 'matching condition,' and gives $Kk_0\bar{r}_0 \approx \gamma\bar{\theta}_0$ [1]. This condition determines an electron beam radius of $r_e = \sqrt{\gamma\varepsilon_n\lambda/\sqrt{2}\pi K}$ where $\lambda = 2\pi/k$ is the optical wavelength. A beam matched in this way gives a phase velocity spread of $\Delta v = 2\pi NKk\varepsilon/\gamma$. Since the phase velocity spread must be less than the gain band-width, $\Delta v \leq 2\pi$, an upper limit on the allowable emittance is $\varepsilon^{max} \leq \gamma\lambda/2\pi NK$.

There have been many approaches to understanding how the FEL works. Among the methods used to develop FEL theory has been a quantum mechanical approach, the use of quantum electrodynamics , the application of plasma physics theories, and the use of plasma physics many-particle computer codes [1]. Early on in the theoretical development, it was shown that a classical approach provided an accurate description of the FEL [7]. The classical approach using a charged-particle current driving Maxwell's equations will be presented here.

B. ELECTRON DYNAMICS

The only significant force acting on an electron as it travels the length of the undulator is the Lorentz force given by the relativistic equations [1]

$$\frac{d(\gamma\bar{\beta})}{dt} = \frac{-e}{mc}\left(\bar{E}_r + \bar{\beta} \times \left(\bar{B}_r + \bar{B}_u\right)\right) \qquad (2\text{-}4)$$

$$\frac{d\gamma}{dt} = \frac{-e}{mc}\left(\bar{\beta} \cdot \bar{E}_r\right) \qquad (2\text{-}5)$$

$$\gamma^{-2} = 1 - \bar{\beta} \cdot \bar{\beta} \qquad (2\text{-}6)$$

where $\bar{\beta} = \bar{v}/c$ is the electron's normalized velocity, $\bar{B}_u = B[\cos(k_0 z), \sin(k_0 z), 0]$ is the helical undulator magnetic field, $\bar{E}_r = E[\cos\psi, -\sin\psi, 0]$ and $\bar{B}_r = E[\sin\psi, \cos\psi, 0]$ are the optical electric and magnetic fields, $\psi = kz - \omega t + \phi$, $k = 2\pi/\lambda$ is the optical wavenumber, $\omega = ck$ is the optical frequency, and ϕ is the phase of the optical wave. Equations of motion for the electrons are obtained by inserting the electric and magnetic fields into the equations above. The plane wave form for the electric and magnetic fields is

9

accurate near the axis of the undulator. Since there are a total of five equations above, and only four unknowns, $\left[\bar{r}(t), \gamma(t)\right]$, one of the equations, the z component of equation (2-4), will be ignored. Expanding the remaining equations yields

$$\frac{d\left(\gamma\bar{\beta}_\perp\right)}{dt} = \frac{-e}{mc}\left[E(1-\beta_z)\left[\cos\psi, -\sin\psi, 0\right] + \beta_z B\left[-\sin(k_0 z), \cos(k_0 z), 0\right]\right] \quad (2\text{-}7)$$

$$\frac{d\gamma}{dt} = \frac{-eE}{mc}\left(\beta_x \cos\psi - \beta_y \sin\psi\right) \quad (2\text{-}8)$$

$$\gamma^{-2} = 1 - \bar{\beta}_\perp^2 - \bar{\beta}_z^2 \quad (2\text{-}9)$$

where $\bar{\beta}_\perp = \left[\beta_x, \beta_y, 0\right]$ is the transverse electron velocity. Since the electrons in an FEL are relativistic, $v_z \approx c$, we have $(1-\beta_z)E \ll \beta_z B$, so that the transverse optical force is much smaller than the undulator field force. This removes the first term on the right side of equation (2-7). The remaining term can be directly integrated yielding

$$\bar{\beta}_\perp = \frac{-K}{\gamma}\left[\cos(k_0 z), \sin(k_0 z), 0\right] \quad (2\text{-}10)$$

The constants of integration are taken to be zero representing an electron beam that is injected perfectly into helical orbits.

The transverse amplitude of the electrons can be found from integrating equation (2-10) further. First, assume that $\gamma(t)$ is a constant, which is a good approximation for low efficiency FELs. Next, assume that $z \approx \beta_0 ct$, so that the electron oscillation frequency in the undulator is $\omega_0 = k_0\beta_0 c$. The arguments within the trigonometric functions of Equation (2-10) can then be rewritten as $k_0 z \approx \omega_0 t$. Integrating now leads to

$$\bar{x}_\perp \approx \frac{K\lambda_0}{2\pi\gamma}\left[-\sin(\omega_0 t), \cos(\omega_0 t), 0\right] \quad (2\text{-}11)$$

10

which yields a transverse amplitude of oscillation, $\Delta x_\perp \approx K\lambda_0/2\pi\gamma$.

Continuing with pendulum equation derivation, substitute equation (2-10) into the energy equation (2-8). Using a trigonometric identity leads to

$$\frac{d\gamma}{dt} = \frac{eEK}{\gamma mc}\cos\big((k_0 + k)z - \omega t + \phi\big). \qquad (2\text{-}12)$$

The electron's phase is identified in equation (2-12) as $\zeta = (k + k_0)z - \omega t$. We see from equation (2-12) that electron phases such that $-\pi/2 < \zeta + \phi < \pi/2$ will gain energy from the radiation, while electron phases such that $\pi/2 < \zeta + \phi < 3\pi/2$ will lose energy to the radiation.

Differentiating the electron phase velocity twice yields $\ddot{\zeta} = (k + k_0)\dot{\beta}_z c$. Inserting the magnitude of equation (2-10) into the definition of γ from equation (2-9) and differentiating with respect to time yields $\dot{\gamma}/\gamma = \gamma^2\beta_z\dot{\beta}_z$. Combining these equations with equation (2-12) gives the pendulum equation

$$\ddot{\zeta} = \frac{2ek_0KE}{\gamma^2 m}\cos(\zeta + \phi) \qquad (2\text{-}13)$$

which governs the electron's motion in the presence of the combined radiation and undulator fields. Defining the dimensionless time as $\tau = ct/L$ (so that $\tau = 0 \rightarrow 1$ as the electrons travel from the beginning to the end of the undulator) normalizes equation (2-13) as

$$\overset{\infty}{\zeta}(\tau) = \frac{L^2}{c^2}\frac{2ek_0KE}{\gamma_0^2 m}\cos(\zeta + \phi) = |a|\cos(\zeta + \phi) \qquad (2\text{-}14)$$

where $\overset{\infty}{(..)} = d^2(..)/d\tau^2 = (L/c)^2 d^2(..)/dt^2$ and $|a| = 4\pi NeEKL/\gamma_0^2 mc^2$ is the dimensionless optical field strength. The relativistic Lorentz factor γ in equation (2-13) has been replaced by its initial value γ_0 in equation (2-14) by assuming low efficiency: the energy changes of the electrons are insignificant during the

11

interaction time τ. The electron pendulum equation for a helical undulator (2-14) is appropriate for low and high gain and correctly follows the development of electron bunching. For the linear undulator, $|a|$ should be modified by letting $K \to K(J_0(\xi) - J_1(\xi))$, where J_0 and J_1 are Bessel functions and $\xi = K^2/2(1+K^2)$.

Using the expressions above, a dimensionless phase velocity can be defined by

$$\nu(\tau) = \dot{\zeta} = L\left[(k + k_0)\beta_z - k\right]. \tag{2-15}$$

The electron experiences resonant undulator and radiation field forces when $\nu = 0$. The resonant relationship between the radiation and undulator wavelengths is

$$\lambda = \lambda_0 \frac{1 + K^2}{2\gamma^2}. \tag{2-16}$$

Equation (2-16) shows that the operating wavelength of an FEL can be altered by changing the electron beam energy γ, the undulator wavelength λ_0, or the undulator parameter K.

C. THE SELF-CONSISTENT WAVE EQUATION

While the Lorentz force law governs the evolution of the electron's trajectory, Maxwell's equations govern the evolution of the optical field in the FEL. Spontaneous emission in an FEL oscillator grows to form a classical field with a bandwidth proportional to the inverse of the number of periods in the undulator. This narrow bandwidth implies that the optical wave varies slowly in space and time over one wavelength. This means we may assume ($E' << kE$, $\dot{E} << \omega E$, $\phi' << k\phi$, $\dot{\phi} << \omega\phi$), where $(..)' = d(..)/dz$, and $(\dot{..}) = d(..)/dt$. These

12

assumptions comprise the slowly-varying amplitude and phase approximation (SVAP) [1].

Neglecting transverse effects, the radiation present in the undulator can be taken to be a circularly-polarized plane wave whose vector potential is

$$\bar{A} = \frac{E(t)}{k}[\sin \psi, \cos \psi, 0] \tag{2-17}$$

where $\psi = kz - \omega t + \phi$. Using this vector potential in the Coulomb gauge of the wave equation yields

$$\left(\bar{\nabla}^2 - \frac{1}{c^2}\frac{d^2}{dt^2}\right)\bar{A} \approx 2\left(\frac{\partial E}{\partial z} + \frac{1}{c}\frac{\partial E}{\partial t}\right)[\cos \psi, -\sin \psi, 0]$$
$$-2E\left(\frac{\partial \phi}{\partial z} + \frac{1}{c}\frac{\partial \phi}{\partial t}\right)[\sin \psi, \cos \psi, 0] = \frac{4\pi}{c}\bar{J}_\perp \tag{2-18}$$

where the SVAP approximation has been used to eliminate all terms with two derivatives. The total beam current density $\bar{J}_\perp$ is the sum of all the single particle currents $\bar{J}_{\perp i} = -ec\bar{\beta}_\perp \delta^{(3)}(\bar{x} - \bar{r}_i)$, where $\bar{r}_i$ is the trajectory of the ith electron and $\bar{\beta}_\perp$ is given in equation (2-10). The fast rotating sine and cosine functions of ψ can be eliminated by defining two orthogonal unit vectors $\hat{\varepsilon}_1 = [\cos \psi, -\sin \psi, 0]$ and $\hat{\varepsilon}_2 = [\sin \psi, \cos \psi, 0]$. Projecting (2-18) onto these two unit vectors separates the wave equation into two first-order scalar differential equations

$$\frac{\partial E}{\partial z} + \frac{1}{c}\frac{\partial E}{\partial t} = \frac{2\pi}{c}\bar{J}_\perp \cdot \hat{\varepsilon}_1 \tag{2-19}$$

and

$$E\left(\frac{\partial \phi}{\partial z} + \frac{1}{c}\frac{\partial \phi}{\partial t}\right) = \frac{2\pi}{c}\bar{J}_\perp \cdot \hat{\varepsilon}_2 \tag{2-20}$$

13

Making the change in coordinates $z = \bar{z} + ct$ in equations (2-19) and (2-20) simplifies the differential operator to $\left(\partial/\partial z + c^{-1}\,\partial\,\partial t\right) \rightarrow c^{-1}\,\partial/\partial t$. The new coordinate $\bar{z}$ stays with a point on the field envelope traveling at speed c. The electrons then drift back with a relative speed $c\left(1 - \bar{\beta}_z\right)$. Inserting this change, as well as the expression for the current density, yields

$$\frac{\partial E}{\partial t} = -\frac{2\pi e K c}{\gamma} \cos\left(\psi + k_0 z\right)\delta^3\left(\bar{x} - \bar{r}_i\right) \qquad (2\text{-}21)$$

and

$$E\frac{\partial \phi}{\partial t} = \frac{2\pi e K c}{\gamma} \sin\left(\psi + k_0 z\right)\delta^3\left(\bar{x} - \bar{r}_i\right). \qquad (2\text{-}22)$$

Next we substitute $\psi + k_0 z = \zeta + \phi$.

A volume element much smaller than the coherence volume, but larger than one wavelength of light, is selected to sample electrons. Since the fields are slowly varying, only one wavelength of phase space is selected and sampled from this volume element, because all wavelengths in the volume must evolve in the same way [1]. The electrons in one wavelength of phase space are sampled to achieve an accurate representation of initial phase space distribution, so the sum over all particles in equations (2-21) and (2-22) can be replaced by an average over the sampled electrons weighted by the electron density ρ [1]. Indicating the ensemble average of particles at a site z by $\langle ..\rangle$, the optical wave equations become

$$\frac{\partial E}{\partial t} = -\frac{2\pi e K c \rho}{\gamma} \langle\cos(\zeta + \phi)\rangle \qquad (2\text{-}23)$$

and

$$E\frac{\partial \phi}{\partial t} = \frac{2\pi e K c \rho}{\gamma} \langle\sin(\zeta + \phi)\rangle. \qquad (2\text{-}24)$$

Finally, by introducing the dimensionless time $\tau = ct/L$, current density $j = 8N(e\pi KL)^2 \rho / \gamma_0^3 mc^2$, and field strength $|a| = 4\pi NeEKL/\gamma_0^2 mc^2$, equations (2-23) and (2-24) further simplify to

$$|\overset{\circ}{a}| = -j\langle \cos(\zeta + \phi)\rangle, \qquad \overset{\circ}{\phi} = \frac{j}{|a|}\langle \sin(\zeta + \phi)\rangle. \qquad (2\text{-}25)$$

In low efficiency FELs, the energy loss per electron within the undulator is small, and so we hold the electron's energy constant at its initial value of γ_0. In complex notation, the wave equation is

$$\overset{\circ}{a} = -j\langle e^{-i\zeta}\rangle, \qquad (2\text{-}26)$$

where $a = |a|e^{i\phi}$ [1]. Equations (2-25) and (2-26) show that electron phases near $\zeta + \phi \approx \pi$ drive the optical amplitude and lead to gain, while the optical phase is driven by electron phases near $\zeta + \phi \approx \pi/2$. These equations complete the feedback mechanism of the FEL. The pendulum equation describes the bunching of electrons which drives the optical amplitude, and the optical amplitude controls the amount of bunching that takes place. For the linear undulator, the dimensionless current j is modified by letting $K \rightarrow K(J_0(\zeta) - J_1(\zeta))$ where J_0 and J_1 are Bessel functions and $\zeta = K^2/2(1 + K^2)$.

The previous derivation of the wave equation disregarded the transverse evolution of the fields by making the plane-wave approximation. To include these transverse diffraction effects, the three-dimensional FEL wave equation uses the SVAP approximation in a similar manner to equations (2-26) and results in the parabolic wave equation [8]

$$\left(\frac{-i}{4}\overline{\nabla}_\perp^2 + \frac{\partial}{\partial\tau}\right)a(\overline{x}, \tau) = -\langle je^{-i\zeta}\rangle, \qquad (2\text{-}27)$$

where $\bar{\nabla}_{\perp}^2 = \partial_x^2 + \partial_y^2$, and transverse coordinates are normalized to the characteristic mode size, so that $x(\pi/L\lambda)^{1/2} \to x$, and $y(\pi/L\lambda)^{1/2} \to y$, and the longitudinal coordinate is $(z - ct)/N\lambda \to z$. Equation (2-27) can be used to include the effects of electron beam radius and diffraction effects.

D. FEL DIMENSIONLESS PARAMETERS

Dimensionless parameters are extremely useful when discussing FEL attributes. Several of them have already been defined and used, such as the undulator parameter K, the electron phase and phase velocity ζ and ν, the current density j, and the optical field a.

The general method of normalizing consists of finding characteristic lengths and times, used as divisors to remove all dimensions. The characteristic time scale is given by the time for an electron to traverse the undulator, L/c. The characteristic longitudinal length for macroscopic processes is the undulator length, L. The characteristic transverse macroscopic length is the optical mode waist size [1]. The characteristic microscopic longitudinal distance is the slippage distance, or the distance that light passes over an electron bunch as it travels down the undulator. Looking at an electron - photon race down the undulator, the photon beats the electron by a distance $\Delta s = \Delta v \cdot \Delta t = (c - \beta_z c) L/c = (1 - \beta_z) N\lambda_0$. Using $(1 - \beta_z) \approx (1 + K^2)/2\gamma^2$, for relativistic electrons combined with the resonance condition (2-16), the slippage distance can be written as $\Delta s \approx N\lambda$. The slippage distance is the characteristic length over which an electron and photon can exchange energy.

Finally, the Rayleigh length, Z_0, is a measure of the optical beam diffraction [1] and is determined by the resonator configuration including mirror separation and curvature. The optical mode waist is related to the Rayleigh length by

$\pi W_0^2 = \lambda Z_0$. The dimensionless Rayleigh length is given by $z_0 = Z_0/L$ [1], and the optical mode waist is normalized by $\sqrt{L\lambda/\pi}$ so that $w_0 = \sqrt{z_0}$.

III. QUANTUM LIMITATION ON FREE ELECTRON LASER START-UP

A. INTRODUCTION

A natural place to begin examining the FEL is at start-up. This chapter looks into processes that occur during the first few passes of the electrons through the undulator. For special FEL designs, the number of photons in the resonator may be few enough to cause quantum mechanical effects in this otherwise classical laser.

On each pass through the FEL oscillator, the periodic magnetic fields of the undulator give the electron a transverse acceleration, causing it to spontaneously emit radiation into the resonator modes [9]. On subsequent passes through the oscillator, the electrons continue to spontaneously emit radiation, but now in the presence of existing radiation. This results in stimulated emission and absorption of photons by the electrons. As the number of photons in the resonator increases sufficiently to describe a classical field, the radiation frequencies with the largest gain grow to dominate the resonator mode and the spectrum narrows. If the single-pass gain of the FEL is above the resonator losses (the "threshold condition"), the radiation power grows exponentially to saturation in strong fields. For most operating FELs, the start-up process occurs in a few hundred passes. However, a new class of compact FELs with short undulator periods λ_0, a large number of periods N, and a low undulator parameter $K = e\bar{B}\lambda_0/2\pi mc^2$, may experience significant delays in start-up due to large fluctuations caused by the low number of photons spontaneously emitted into the resonator mode each pass. In some cases, the

18

FEL reaches steady-state without sufficient photons to achieve a classical field, and the FEL fails to operate.

B. COMPACT FEL DESCRIPTION

Compact FELs are a new, exciting direction in FEL research and offer attractive advantages over conventional FELs in several ways. The compact FEL has a significantly reduced undulator period, $\lambda_0 \approx 1mm$, which should reduce the size, weight, and cost of the FEL. The shorter undulator period also allows production of a short wavelength radiation with a less powerful accelerator, since the radiation wavelength is inversely proportional to the electron beam energy γmc^2, $\lambda = \lambda_0 (1 + K^2)/2\gamma^2$. Unfortunately, decreasing the undulator period reduces the coupling of the electrons to the transverse radiation field, since the deflection of the electrons in the undulator is given by $\Delta x \approx K\lambda_0/2\pi\gamma$. To make matters worse, there are technological problems with obtaining high magnetic field densities in very short undulator periods, thereby reducing the undulator parameter to a value $K << 1$. This problem acts to further reduce the gain. The length $L = N\lambda_0$ of the compact undulator must be increased to compensate for the reduced gain.

The accelerator used by the compact FEL to produce short wavelength radiation may be much less energetic than that required by a typical FEL since the undulator period is reduced. But, because the compact FEL has an increased number of periods, the accelerator must have higher beam quality consistent with the decreased gain spectrum bandwidth, $1/(2N)$. In this analysis, the beam quality is considered achievable, so that neither emittance nor energy spread degrades the FEL gain. In this compact FEL design, the undulator period is small which leads to a small undulator parameter $K << 1$. A

19

large number of undulator periods are used to insure the expected classical gain is above the threshold condition.

C. START-UP OF THE COMPACT FEL

On each pass through the undulator, the number of spontaneously emitted photons from a single electron into the resonator mode is calculated as follows. The total power radiated by a single electron is given by [10]

$$P = \frac{2e^2 \gamma^4 \dot{\beta}_\perp^2}{3c} \qquad (3\text{-}1)$$

where $\dot{\beta}_\perp = K k_0 c / \gamma$ is the electron's transverse acceleration. The energy of a photon emitted at the radiation frequency satisfying the resonance condition, $\omega = 2\gamma^2 k_0 c$, is

$$E \approx 2\hbar c k_0 \gamma^2. \qquad (3\text{-}2)$$

The number of photons emitted by one electron in one pass through the undulator is then obtained by multiplying the power equation (3-1) by the time an electron spends in the undulator, $\Delta t \approx L/c$, and then dividing by the photon energy to obtain

$$W_T = 2N\alpha K^2. \qquad (3\text{-}3)$$

Here $\alpha = e^2/\hbar c$ is the fine structure constant.

The quantity in equation (3-3) is the number of photons emitted into the solid angle γ^{-2} [10]. As Figure 3-1 shows, this solid angle is typically large enough so that most photons miss the mirror at the ends of the resonator and are lost. In order to calculate the fraction of the photons captured in the resonator, we

must multiply W_T by the ratio of the solid angle subtended by the fundamental resonator mode.
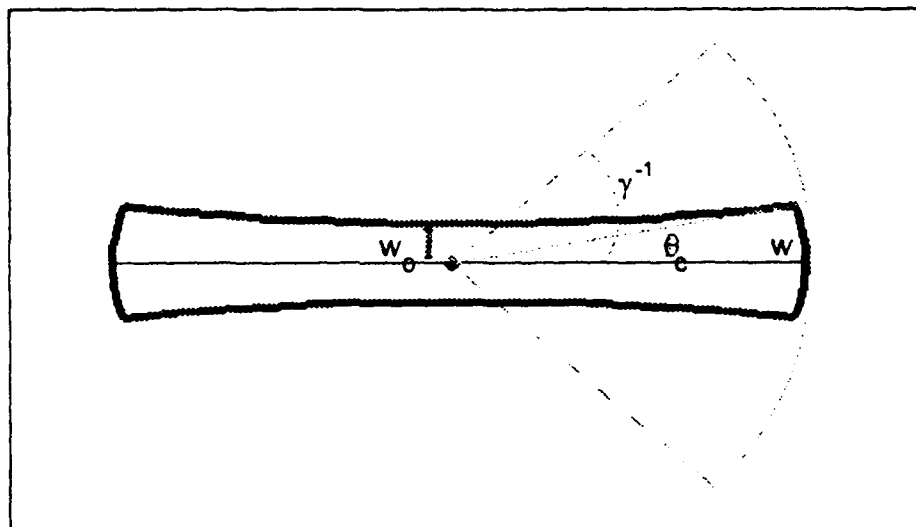

Figure 3-1. Diagram showing relative sizes of the emission angle γ^{-1} and the largest angle at which photons can be stored within the resonator, θ_c.

The optical mode radius is given by $w^2 = w_0^2(1 + z^2/z_0^2)$, where w_0 is the optical mode waist, $z_0 = \pi w_0^2/\lambda$ is the Rayleigh length, so that the solid angle subtended by the optical mode is $\approx 1/(2N\gamma^2)$. Multiplying the number of photons emitted by an electron per pass, W_T, by the ratio of solid angles gives $W_\gamma = \alpha K^2$ [3] as the number of photons emitted per pass that are saved in the resonator mode.

Each electron in the beam emits W_γ photons into the resonator mode. The volume, $V_c \approx N^2 \lambda^2 \lambda_0$, is used to count electrons and photons and is determined by a longitudinal length corresponding to the gain bandwidth $N\lambda$, and the transverse mode area $L\lambda = N\lambda\lambda_0$ [1]. The number of photons spontaneously emitted in one pass into this volume is $S_\gamma = \rho F \alpha K^2 N^2 \lambda^2 \lambda_0$ where ρ is the electron beam particle density, $F = \pi r_b^2/\pi w_0^2$ is the filling factor describing the transverse overlap of the electron and optical beams, r_b is the electron beam radius, and $w_0 \approx (L\lambda/3\pi)^{1/2}$ is the radiation mode waist.

21

After a few passes, there are N_γ photons in the volume V_c. The resulting radiation field follows a Poisson distribution giving a fluctuation in the photon number of $N_\gamma^{-1/2}$ [11]. If these fluctuations are larger than the gain bandwidth of the FEL, $1/(2N)$, they act to reduce gain. To include the effect of these photon fluctuations we consider a simple analogy. Since the dimensionless radiation field is given by $|a| = 4\pi NeKLE/\gamma_0^2 mc^2$, where E is the radiation's electric field, a fractional fluctuation in E is equivalent to a fractional fluctuation in the undulator parameter K. Thus, to the electron, the radiation fluctuations are equivalent to an imperfect undulator field of $N_\gamma^{1/2}$ coherent periods. Clearly, $N_\gamma^{1/2} \approx N$ signals the presence of a classical field within the resonator. The gain in the undulator is proportional to the dimensionless current density $j = 8N^3(e\pi K\lambda_0)^2 \rho F/\gamma_0^3 mc^2$, although j must be corrected by the ratio $\left(N_\gamma^{1/2}/N\right)^3$ for the calculated gain to account only for the coherent number of periods in the undulator. However, there are $\left(N/N_\gamma^{1/2}\right)$ coherent undulators acting in series. Thus, the actual gain per pass after one pass, including quantum fluctuations, is estimated as

$$G = G_0 \frac{N_\gamma}{N^2}, \qquad (3\text{-}4)$$

where $G_0 \approx 0.135 j$ is the classical small-signal gain. If the number of photons spontaneously emitted on the first few passes is low, the photon fluctuations may be large and lead to a significant decrease in gain.

After many passes, the number of photons in the resonator will change due to continued spontaneous emission, the resonator Q losses, and possible gain from stimulated emission. The differential equation describing the evolution of the photon number, N_γ, over many passes, n, is [11]

$$\frac{dN_\gamma}{dn} = S_\gamma + N_\gamma\left(G - Q^{-1}\right), \tag{3-5}$$

where Q represents the loss within the resonator. The FEL may remain below threshold, $G < Q^{-1}$, and yield a steady state when the number of photons reaches

$$N_\gamma^{\ *} = \frac{N^2}{2G_0 Q}\left[1 \pm \left(1 - \frac{4S_\gamma G_0 Q^2}{N^2}\right)^{1/2}\right]. \tag{3-6}$$

Equation (3-6) shows the possibility of a complex number of photons, which can be interpreted as the absence of a steady-state solution and no start-up of the FEL. From this interpretation, it is inferred that the start-up condition is $4S_\gamma G_0 Q^2 / N^2 > 1$. Substituting $S_\gamma = \rho F \alpha K^2 N^2 \lambda^2 \lambda_0$, the dimensionless current density j, the small signal gain $G_0 \approx 0.135 j$, and introducing the Compton wavelength $\lambda_c = \hbar/mc$ leads to a general start-up condition

$$0.135(jQ)^2 \lambda\gamma > (2\pi)^2 N^3 \lambda_c. \tag{3-7}$$

In the classical limit, $\lambda_c \to 0$, all FELs satisfy this requirement and start. A typical FEL (such as the original Stanford SCA/FEL designed with $jQ \approx (4\pi)^2$, Lorentz factor $\gamma \approx 80$, $\lambda = 3\mu m$, and $N = 160$) satisfies the requirement of equation (3-7) by two orders of magnitude.

On the other hand, a compact FEL with parameters of $\gamma \approx 24$, $\lambda = 86\mu m$, $jQ \approx 70$, and $N = 10^3$ results in no start-up. Two figures, 3-2 and 3-3, appear below. Figure 3-2 represents the results of a conventional ("classical") calculation which does not include quantum fluctuations. This calculation and that figure erroneously predict successful start-up. Figure 2-3, which does include quantum fluctuations, correctly predicts that the FEL does not start up.

23

The numerical simulation including the classical spontaneous emission line spectrum is used to determine the photon evolution per pass without the quantum fluctuation term included in the spectrum. The bottom panel shows the classical spontaneous emission spectrum while the middle panel shows the photon number evolution over n=300 passes with the final spectrum at the top. Over a few passes, the photon number spectrum shifts to the maximum gain frequency and narrows to a classical FEL line spectrum. The gain spectrum $G\gamma$ is displayed with the dotted line showing the loss per pass. The total number of photons spontaneously emitted per pass is given by $S_\gamma = 278$. The total number of photons in the final laser spectrum is $N_{\gamma_f} = 2.9 \times 10^{15}$. Normally, high-power saturation would limit the final number of photons to a value less than N_{γ_f} before $n = 300$ passes, but high-power saturation is not included in this simulation.

$$\delta N_\gamma(v) = S_\gamma(v) + N_\gamma(v) \, [G(v) - 1/Q]$$

Coherence Evolution
j= 0.813   Q=90
K=0.01   N=1000
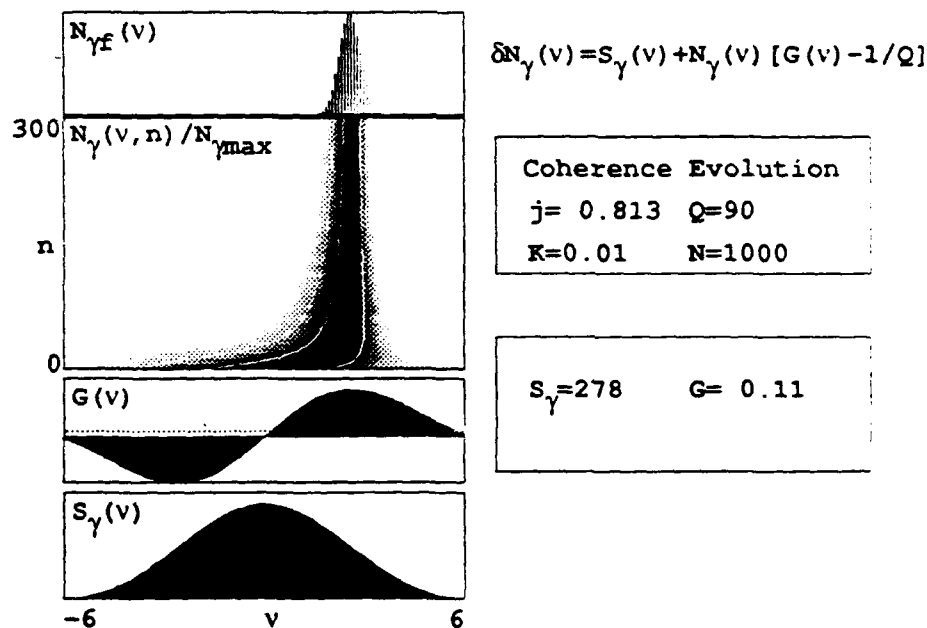
S_γ=278   G= 0.11

Figure 3-2. Photon number evolution using small-signal gain.

Figure 3-3 displays the results of including quantum fluctuations in the gain term. After $n=2000$ passes, the upper panel shows the photon number spectrum begins to increase in amplitude and evolve toward the maximum gain frequency. Before reaching the threshold, a steady state is reached with $N_{\gamma_f} = 2.7 \cdot 10^4$ photons, where the increase in photons per pass due to spontaneous emission $S_\gamma = 278$, and stimulated emission GN_γ, is equal to the losses in the system, QN_γ. The actual gain of the laser, including the quantum fluctuation term, is below the losses of the laser, as shown in the center panel. Although this compact FEL would be expected to work according to classical FEL theory, Figure 3-3 shows a steady state photon number is reached in the resonator below that required for a classical field. Thus, the gain never exceeds the losses and the laser does not start.

$$\delta N_\gamma(\nu) = S_\gamma(\nu) + N_\gamma(\nu)[G(\nu) - 1/Q]$$
$$G(\nu) = 0.135 j(N_\gamma /N^2)$$

Coherence Evolution

j= 0.813	Q=90
K=0.01	N=1000

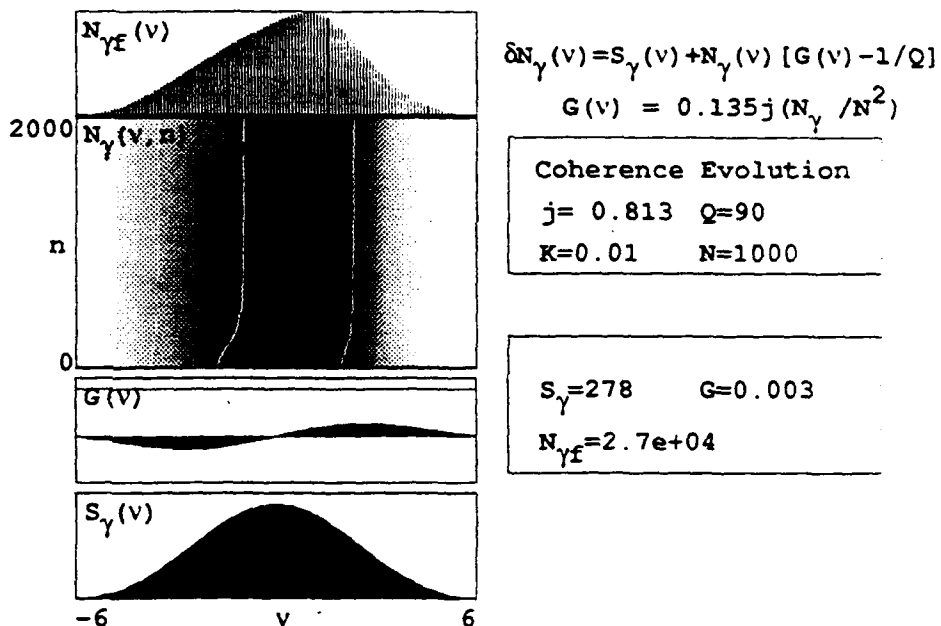| S_γ=278	G=0.003
N_{γ_f}=2.7e+04	

Figure 3-3. Photon number evolution using the modified equation (3-4) as the gain.

D. ANALYTICAL RESULTS

Assuming a form for the gain of $G \approx G_0 N_\gamma / N^2$, the photon rate equation (3-5) can be solved analytically for the photon number evolution per pass. Again, this solution is valid only up to $N_\gamma = N^2$ at which time the model used to develop the gain formula is no longer valid. The solution separates into two cases: one when the start-up condition (3-7) is satisfied, and the other when it is not. If the start-up condition is not satisfied, the photon number after the nth pass is given by

$$N_\gamma = \frac{N^2}{2G_0Q}\left[1 + q\left(1 + \frac{2r}{e^{-nq/Q} - r}\right)\right],\qquad(3\text{-}8)$$

where $q = \left(1 - 4G_0 S_\gamma Q^2 / N^2\right)^{\frac{1}{2}}$ and $r = \left|(1+q)/(q-1)\right|$. This solution displays a linear growth dependence on n for small n. However, there are never enough photons in the resonator for the gain to overcome FEL loss defined by Q, so a steady-state is reached with an insufficient number of photons in the resonator to form a classical field. If the start-up condition (3-7) is satisfied, the photon number after the nth pass is

$$N_\gamma = \frac{N^2}{2G_0Q}\left(\frac{p \cdot tan\left(\frac{np}{2Q}\right) - 1}{1 + \frac{1}{p} \cdot tan\left(\frac{np}{2Q}\right)} + 1\right),\qquad(3\text{-}9)$$

where $p = \left(4G_0 S_\gamma Q^2 / N^2 - 1\right)^{\frac{1}{2}}$. This solution for the photon number evolution grows slowly per pass initially due to contributions primarily from spontaneous emission. As the number of photons in the resonator grows, stimulated emission begins to add photons and their number increases dramatically. This continues

until the fluctuations in photon number are much less than the gain spectrum bandwidth resulting in classical gain.

The threshold for which stimulated emission produces as many photons as does spontaneous emission is obtained by setting $S_\gamma = N_\gamma G$. Dattoli [12] gives an expression for this threshold number of photons as $(N_\gamma)_{th} = \gamma\lambda/(32\pi^2 N\lambda_c)$ using a quantum mechanical formalism. This expression can be reproduced with all the correct functional proportionalities much more simply by setting the gain equal to the small signal gain $G = 0.135j$. However, when quantum fluctuations are included, and the gain is determined by (3-4), the condition for the stimulated emission to equal the spontaneous emission is

$$(N_\gamma)_{th} \approx \left(\frac{N\lambda\gamma}{2\pi^2\lambda_c}\right)^{1/2}.$$

(3-10)

This new condition is different from Dattoli's and takes into account the reduced gain initially present due to fluctuations in the radiation field. It can be seen that if the laser start-up condition is not fulfilled, the steady-state photon number within the resonator, N_γ^*, will be less than the threshold number of photons required for equal spontaneous and stimulated emission rates.

E. CONCLUSIONS AND FURTHER RESEARCH SUGGESTIONS

The type of FEL that may exhibit start-up problems due to quantum fluctuations is one that attempts to produce short optical wavelengths with a low energy electron beam. The low energy electron beam necessitates a small period undulator, which in turn reduces the undulator parameter. Both of these properties act to reduce the expected gain of the FEL. In order to achieve

27

sufficient gain, the number of periods in the undulator must be increased. However, this design logic can lead to an FEL that may not operate due to quantum fluctuations during start-up.

IV. ANALYTICAL DESCRIPTION OF LONGITUDINAL MODES

A. INTRODUCTION

The optical power in the FEL oscillator starts from spontaneous emission and grows to strong-field saturation over many passes. During the crucial startup process, coherence develops in the weak optical field and small microscopic bunching develops in the electron beam. In this chapter the FELs considered are typical in the sense that the quantum effects previously explored do not occur. The FELs considered here have weak classical fields, low gain, and electron pulses much longer than the slippage distance $N\lambda$.

Assuming low gain, a long pulse, and weak optical fields, Elleaume [12] showed that FEL optical pulse evolution could be described by a Schroedinger-type equation with a non-Hermitian harmonic oscillator Hamiltonian . Using the same assumptions, Dattoli [13.14,15,16] employed methods of quantum optics and an integro-differential equation to obtain his solution to the same problem. In each case, the mathematical result involves second-order derivatives. In this chapter, we expand the optical and electron pulse shapes in a Taylor series to derive a first-order partial-differential equation describing the optical field evolution over many passes through the undulator. This equation is used to investigate coherence development and the effects of the electron pulse shape on the optical field amplitude and phase.

B. MATHEMATICAL DEVELOPMENT

In order to generalize the optical field in the longitudinal direction, to allow for multiple optical modes, we must follow the optical field envelope evolution all along z. The extension to multi-mode theory by transforming $a \rightarrow a(z)$ is equivalent to allowing the optical field a continuum of wavenumbers $a \rightarrow a(k)$. Fully extending the theory uses $a \rightarrow a(z)$, $v \rightarrow v(z)$, and $\zeta \rightarrow \zeta(z)$.[1] As discussed in Chapter II, all longitudinal distances are normalized to the slippage distance, the distance over which the light and electrons can exchange information, so that $z/N\lambda \rightarrow z$. The electrons slip back one slippage distance, or $\Delta z = 1$, with respect to the light during the interaction time $\tau = 0 \rightarrow 1$ leading to $N\lambda = \Delta z = \tau$.

The FEL interaction can be described by the optical wave equation [1],

$$\overset{\circ}{a}(z, \tau) = j\sigma(z + \tau)\left\langle exp\left[-i\zeta(z + \tau, \tau)\right]\right\rangle \qquad (4\text{-}1)$$

coupled to the electron pendulum equation [1],

$$\overset{\circ\circ}{\zeta}(z, \tau) = \overset{\circ}{v}(z, \tau) = \left|a(z - \tau, \tau)\right|cos\left[\zeta(z, \tau) + \phi(z - \tau, \tau)\right], \qquad (4\text{-}2)$$

where $(..) = d(..)/d\tau$, $\zeta = (k + k_0)z - \omega t$ is the electron phase, $v = L[(k + k_0)\beta_z - k] = \overset{\circ}{\zeta}$ is the electron phase velocity, $\left|a(z, \tau)\right|$ is the optical electric field amplitude, $\phi(z, \tau)$ is the optical phase, and $<..>$ represents an average over all of the electrons in the beam. The electrons' pulse shape is described by $\sigma(z)$ with peak value of unity. The longitudinal field sites z refer to positions on the optical field envelope. In (4-1), the light remains fixed in z while the electrons slip back to a field site $z + \tau$, while in (4-2), the electrons remain fixed and the light slips ahead by $z - \tau$ as it moves through the undulator. This

slippage allows the light and electrons to exchange information, and allows the electrons to transfer of information from one optical site to another.[1]

When the FEL is operating in the low-gain regime, we expand equation (4-1) to lowest order in the current density, j, and assume the field changes are small over a single pass, $\overset{\circ}{a}| << |a|$ and $\overset{\circ}{\phi} << \phi$. Since the optical fields are weak, the electron phase may be expanded to lowest order in the field magnitude $|a|$, giving $\zeta = \zeta_0 + v_0\tau + ...$. Here ζ_0 is the initial electron phase, and v_0 is the initial electron phase velocity. The long pulse shapes may be expanded in a Taylor series in the normalized slippage distance, τ: $\sigma(z + \tau) = \sigma(z) + \tau\sigma'(z) + ...$, $|a(z - \tau)| = |a(z)| - \tau|a(z)|' + ...$ and $\phi(z - \tau) = \phi(z) - \tau\phi'(z) + ...$ where $(..)' = d(..)/dz$. These assumptions allow the expansion and integration of equation (4-2),

$$
\zeta(z + \tau, \tau) = \zeta_0 + v_0\tau + \frac{|a|}{v_0^2}\left[-\cos(\zeta_0 + v_0\tau + \phi) + \cos(\zeta_0 + \phi) - v_0\tau\sin(\zeta_0 + \phi)\right]
$$
$$
- \frac{|a|'}{2v_0^3}\left[2\sin(\zeta_0 + v_0\tau + \phi) - 2\sin(\zeta_0 + \phi) - 2v_0\tau\cos(\zeta_0 + \phi)v_0^2\tau^2(\zeta_0 + \phi)\right]
$$
$$
+ \frac{|a|\phi'}{v_0^3}\left[2\cos(\zeta_0 + v_0\tau + \phi) - 2\cos(\zeta_0 + \phi) - 2v_0\tau\sin(\zeta_0 + \phi) + v_0^2\tau^2\cos(\zeta_0 + \phi)\right]
$$
$$
+ ......, \tag{4-3}
$$

where $|a| = |a(z)|$, $|a|' = |a(z)|'$, $\phi = \phi(z)$, and $\phi' = \phi'(z)$.

For a monoenergetic beam (where all electrons have the same initial phase velocity, v_0) the electron dynamics expressed in equation (4-3) can be incorporated into the optical field equation (4-1) using the phase average $\langle .. \rangle = \int_0^{2\pi}(..)d\zeta_0 / 2\pi$. The complex optical field equation then becomes

$$\frac{da}{d\tau} = j\sigma\left[\left(ia + \frac{a'}{v_0}\right)\left[\frac{1 - e^{-iv_0\tau} - iv_0\tau e^{-iv_0\tau}}{v_0^2}\right] - \frac{ia'}{2v_0}\tau^2 e^{-iv_0\tau}\right]$$
$$+ iaj\tau\sigma'\left[\frac{1 - e^{-iv_0\tau} - iv_0\tau e^{-iv_0\tau}}{v_0^2}\right] \qquad (4\text{-}4)$$

where $a = |a(z)|\exp(i\phi(z))$. This equation includes the electron dynamics of equation (4-2) using the assumption of low gain, weak fields, and long pulses as expressed in equation (4-3).

Integrating over a single pass, $\tau = 0 \rightarrow 1$, yields the following partial-differential equation for the net change, Δa, in the complex optical field,

$$\Delta a = ja\sigma g(v_0) - \frac{i}{2}ja\frac{\partial\sigma}{\partial z}h(v_0) - \frac{i}{2}j\sigma\frac{\partial a}{\partial z}g'(v_0) \qquad (4\text{-}5)$$

with constant coefficients for a given initial electron phase velocity

$$g = \frac{2 - 2e^{-iv_0} - iv_0(1 + e^{-iv_0})}{2v_0^3}, h = \frac{6 - 6e^{-iv_0} - 6iv_0e^{-iv_0} + v_0^2(1 + 2e^{-iv_0})}{2v_0^4}, g' = \frac{dg}{dv_0}. \quad (4\text{-}6)$$

With no pulses, $\sigma = 1$ and $a' = 0$ so there are no longitudinal modes. The second and third terms on the right side of equation (4-5) are zero. In that case, equation (4-5) describes the usual single-mode, low-gain evolution of the complex optical field [1]. The real part of $g(v_0)$ is the familiar antisymmetric gain spectrum in v_0, and the imaginary part describes the symmetric shift in the optical phase [1]. The phase velocity v_0 determines the resonance between the optical wavelength, undulator wavelength, and electron z velocity; maximum gain occurs for $v_0 = 2.60616$. The functions $h(v_0)$ and $g'(v_0)$ in (4-5) determine the effects of slippage and the electron pulse shape on the optical field evolution. Elleaume [13] and Dattoli [14,15,16,17] obtained similar functions of v_0 in their

treatment of the long pulse problem, but they also keep some second-order derivatives in the expansion of the field.

Over many passes n through the undulator, the effects of resonator losses and desynchronism must be included [1]. Desynchronism measures the mismatch at the beginning of the undulator between the arrival times of the succession of electron pulses from the accelerator, and the rebounding optical pulse in the resonator cavity. The dimensionless desynchronism is $d = -2\Delta S / N\lambda$, where ΔS is the difference between the actual resonator length and the synchronous cavity length [1]. The resonator loss over many passes is described by the resonator quality factor Q. The resulting first-order partial differential equation gives the development of longitudinal modes in a long pulse over many passes n in weak fields of a low gain FEL,

$$\frac{\partial a}{\partial n} = ja\sigma g(v_0) - \frac{i}{2} ja \frac{\partial \sigma}{\partial z} h(v_0) - \frac{i}{2} j\sigma \frac{\partial a}{\partial z} g'(v_0) - \frac{a}{2Q} - d\frac{\partial a}{\partial z}. \quad (4\text{-}7)$$

The complicated optical pulse evolution determined by equation (4-7) depends only on the dimensionless current j, the resonator Q, the desynchronism d, the electron pulse shape $\sigma(z)$, the initial optical pulse amplitude $|a_0(z)|$ and phase $\phi_0(z)$, and the initial phase velocity v_0.

Since the shape of the phase, $\phi(z)$, is free to evolve, the phase velocity v_0 is somewhat arbitrary. For instance, if the phase has a linear slope, $\phi(z) = \Delta kz$, it is equivalent to a change in wave number, $k \to k + \Delta k$, and alters the effective value of the phase velocity. Therefore, the phase velocity v_0 in equation (4-7) can be chosen for convenience with no loss of generality. A unique and important value of v_0 is the phase velocity giving peak FEL gain, $g_r'(v_0^*) = 0$. The optical pulse will naturally evolve towards $v_0^* = 2.60616$ because of mode

33

competition. In fact, v_0 cannot be chosen far from v_0^*, because the slope of the phase required to evolve to peak gain can exceed the restrictions of the slowly-varying amplitude and phase approximation. This phenomenon can be seen by beginning with the phase velocity $v_0 = L[(k + k_0)\beta_z - k]$ and deriving the change in phase velocity for a change in wave number $\Delta v = -\Delta k = -\phi'$. It can be seen that the slope of the phase provides the change in wave number. Next, using the slowly-varying phase approximation, the change in the slope of the phase must be small as the optical field makes one pass in the undulator, so $\Delta v \Delta \tau \leq 1$. During one pass, the optical phase interacts over a dimensionless distance of Δz which can be linked to the size of the electron pulse σ_z. This in turn gives a new requirement $\Delta v \Delta \sigma_z \leq 1$. Since one of the basic assumptions of this analysis that $\sigma_z \gg 1$, the restriction $\Delta v \ll 1$ is implied. When $v_0 = v_0^*$ and $g_r' = 0$, the equations for the amplitude and phase in (4-7) become uncoupled, and are given by

$$\frac{\partial |a|}{\partial n} + \left(d - \tfrac{1}{2} jg_i'\sigma\right)\frac{\partial |a|}{\partial z} = \left(jg_r\sigma + \tfrac{1}{2}jh_i\sigma' - 1/2Q\right)|a|, \qquad (4\text{-}8)$$

$$\frac{\partial \phi}{\partial n} + \left(d - \tfrac{1}{2}jg_i'\sigma\right)\frac{\partial \phi}{\partial z} = jg_i\sigma - \tfrac{1}{2}jh_r\sigma'. \qquad (4\text{-}9)$$

The equations describing the evolution of the optical amplitude and phase can now be solved separately.

C. ELECTRON PULSE EFFECTS

In this section, three different shapes for the electron pulse are considered and then used to solve equations (4-8) and (4-9) analytically. The method of characteristics [18] will be used to solve equations (4-8) and (4-9).

The left-hand-side of equations (4-8) and (4-9) can be seen to be the directional derivative of $|a(z,n)|$ and $\phi(z,n)$ respectively, in the direction of the vector $\left[1,(d - \frac{1}{2}jg_i'\sigma)\right]$. The equations

$$\frac{dz}{ds} = d - \frac{jg_i'\sigma}{2} \tag{4-10}$$

and

$$\frac{dn}{ds} = 1 \tag{4-11}$$

determine a family of curves $z = z(s)$ and $n = n(s)$ whose tangent vector, $\left[z'(s), n'(s)\right]$, coincides with the vector $\left[1,(d - \frac{1}{2}jg_i'\sigma)\right]$. Therefore, the derivative of $a(z,n)$ along these curves becomes

$$\frac{d|a|}{ds} = \frac{d|a[z(s),n(s)]|}{ds} = \frac{\partial |a|}{\partial z}\frac{\partial z}{\partial s} + \frac{\partial |a|}{\partial n}\frac{\partial n}{\partial s} =$$
$$\frac{\partial |a|}{\partial n} + \left(d - \frac{jg_i'\sigma}{2}\right)\frac{\partial |a|}{\partial z} = \left(jg_r + \frac{jh_i\sigma'}{2} - \frac{1}{2Q}\right)|a|, \tag{4-12}$$

and

$$\frac{d\phi}{ds} = \frac{d\phi[z(s),n(s)]}{ds} = \frac{\partial \phi}{\partial z}\frac{\partial z}{\partial s} + \frac{\partial \phi}{\partial n}\frac{\partial n}{\partial s} =$$
$$\frac{\partial \phi}{\partial n} + \left(d - \frac{jg_i'\sigma}{2}\right)\frac{\partial \phi}{\partial z} = \left(jg_i + \frac{jh_r\sigma'}{2}\right), \tag{4-13}$$

after using the chain rule and equations (4-10) and (4-11). The family of curves $z = z(s)$, $n = n(s)$, and $a(s) = |a(s)|e^{i\phi(s)}$, determined from the solutions of the system of ordinary differential equations (4-10) through (4-12) or (4-10),(4-11), and (4-13) are called the "characteristic curves" of the partial differential equations (4-8) or (4-9) [18]. The approach of solving equations (4-8) or (4-9) by using the solutions of equations (4-10) through (4-12) or (4-10),(4-11), and (4-13) is called the "method of characteristics". The existence and uniqueness

35

theorem assumes certain smoothness conditions on the functions of z and n which guarantee that exactly one solution curve $(z(s), n(s), a(s))$ of equations (4-10) through (4-13) passes through the initial condition point (z_0, n_0, a_0). Using the initial values to create the parametric initial solution curve gives $z = z_0$, $n = 0$, and $|a| = |a_0(z_0)|$ where $|a_0(z_0)|$ is the initial optical field shape and $\phi = \phi_0(z_0)$ where $\phi_0(z_0)$ is the initial optical phase. Equations (4-10) and (4-11) can be solved for z and n as functions of s and z_0. These solutions are then inverted and equations (4-12) and (4-13) are solved and substitutions made to obtain $|a(z,n)|$ and $\phi(z,n)$. The three specific cases follow.

1. Continuous Electron Beam

For the special case of a continuous electron beam, $\sigma(z) = 1$ for all z, at the phase velocity for the peak gain, $\nu_0^{\cdot}$, the optical pulse can still evolve over many passes. The first-order, partial-differential equations (4-8) and (4-9) are solved using the method of characteristics.

Solving equations (4-10) through (4-13) yields

$$z(s, z_0) = z_0 + \left(d - \tfrac{1}{2} j g_i'\right)s, \tag{4-14}$$

$$n(s, z_0) = s, \tag{4-15}$$

$$|a(s, z_0)| = |a(z_0)| \exp\left[\left(jg_r - \frac{1}{2Q}\right)s\right], \tag{4-16}$$

and
$$\phi(s, z_0) = jg_i s + \phi_0(z_0) \tag{4-17}$$

which can be inverted to solve for s and z_0 in terms of n and z. These results are then substituted into the expression for $|a|$ and ϕ to yield solutions for the optical amplitude and phase,

$$|a(z,n)| = |a_0(z_0)| \exp\left[(jg_r - 1/2Q)n\right], \tag{4-18}$$

and

$$\phi(z,n) = jg_i n + \phi_0(z_0), \tag{4-19}$$

where $|a_0(z_0)|$ and $\phi_0(z_0)$ describe the initial optical pulse, $g_r = \text{Re}(g)$ is the real part of $g(\nu_0)$, $g_i = \text{Im}(g)$ is the imaginary part of $g(\nu_0)$, and the position $z_0 = z - (d - \tfrac{1}{2} jg_i')n$ describes the optical pulse centroid shifting over n passes through the resonator due to desynchronism. If $d \leq \tfrac{1}{2} jg_i'$, the optical pulse shifts back over many passes toward the trailing edge of the electron pulse. Further, if $d > \tfrac{1}{2} jg_i'$, the optical pulse shifts forward toward the front edge of the electron pulse. The shape of the optical pulse amplitude and phase remains the same as the initial pulse throughout the evolution. Figure 4-1 shows a comparison of the analytical solution (4-18) and (4-19) with the results of a numerical simulation for the same conditions. The electron pulse is continuous in length with all electrons at phase velocity ν_0^* for maximum gain.
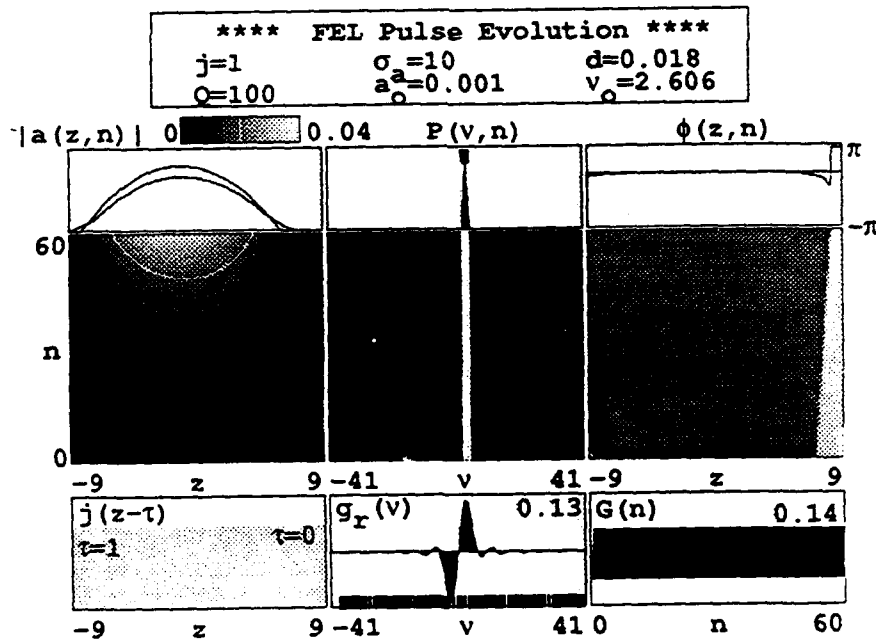

Figure 4-1. Optical pulse evolution comparing a numerical simulation with the analytical solution for a square electron pulse.

37

The desynchronism is $d = 0.018$; the initially weak optical field amplitude is parabolic with a maximum of $a_0 = 0.001$ and a full width of $\sigma_a = 10$; the initial phase is $\phi_0(z) = 0$ for all z; and the resonator loss is determined by $Q = 100$. The lower-left panel displays the continuous electron pulse shape with $\sigma = 1$ for all z. The middle-left panel shows the evolution of the optical pulse over $n = 60$ passes with the final optical field amplitude and shape in the top-left panel. The analytical solution gives a slightly larger amplitude than the numerical simulation, but the centroids and shapes of the two solutions are in close agreement. The middle-right panel shows the evolution of the optical phase over the $n = 60$ passes with the analytical and numerical solutions after the final pass displayed at the top-right. The similarity of the two solutions is quite apparent within the portion of the window occupied by the optical pulse with significant amplitude. In regions where the optical amplitude is small, the optical phase becomes meaningless.

2. Parabolic Electron Beam

The parabolic electron pulse has the form $\sigma(z) = 1 - 2z^2 / \sigma_z^2$ for $|z| < \sigma_z / \sqrt{2}$, and $\sigma(z) = 0$ otherwise. The parabolic electron pulse shape is often used in FEL simulations. In addition, the parabolic equation expresses the same z dependence as the first two terms in a Taylor expansion of any pulse shape. Using the parabolic electron pulse shape, equations (4-8) and (4-9) can be solved analytically for arbitrary initial optical pulse amplitude $|a_0(z)|$, and phase, $\phi_0(z)$ using the method of characteristics.

The solution to equations (4-8) and (4-9) yields results for two cases depending on whether the optical pulse shifts forward due to large desynchronism, $d > \frac{1}{2} jg_i{}'$, or backward due to large gain, $d \leq \frac{1}{2} jg_i{}'$.

38

In the first case, where desynchronism dominates gain, $d > \frac{1}{2} j g_i'$ and the optical pulse tends to shift forward, equations (4-10) through (4-13) yield

$$s = \frac{\sigma_z}{\sqrt{b j g_i'}} \left[tan^{-1}\left(\frac{z(s,z_0)}{\sigma_z} \sqrt{\frac{j g_i'}{b}} \right) - tan^{-1}\left(\frac{z_0}{\sigma_z} \sqrt{\frac{j g_i'}{b}} \right) \right] , \qquad (4\text{-}20)$$

$$n(s,z_0) = s , \qquad (4\text{-}21)$$

$$|a(s,z_0)| = |a_0(z_0)| exp\left[\left(j g_r - \frac{1}{2Q} + \frac{2 g_r b}{g_i'} \right) s \right]$$

$$exp\left[\frac{-2 g_r z}{g_i'} + \frac{2 j g_r b^{1/2} \sigma_z}{(j g_i')^{3/2}} tan(q) \right] \left| \frac{cos\left[tan^{-1}\left(\left(\frac{j g_i z^2}{b \sigma_z^2} \right)^{1/2} \right) \right]}{cos(q)} \right|^{2h_i/g_i'} \qquad (4\text{-}22)$$

$$\phi(s,z_0) = \phi_0 + j g_i s - 2 j g_i \sigma_z \left(\frac{b^{1/2}}{(j g_i')^{3/2}} \right) \left[\left(\frac{j g_i}{b} \right)^{1/2} \frac{z}{\sigma_z} - \frac{s}{\sigma_z} (b j g_i')^{1/2} - tan(q) \right]$$

$$\qquad (4\text{-}23)$$

$$+ \frac{2h_r}{g_i'} ln\left| \frac{cos(q)}{cos\left[tan^{-1}\left((j g_i' z^2 / b \sigma_z^2)^{1/2} \right) \right]} \right| ,$$

where $b = d - \frac{1}{2} j g_i'$ and

$$q = tan^{-1}\left(\left(\frac{j g_i' z^2}{\sigma_z^2 b} \right)^{1/2} \right) - \frac{s}{\sigma_z} (b j g_i')^{1/2} .$$

Substituting equations (4-20) and (4-21) into equations (4-22) and (4-23) gives the optical amplitude

39

$$|a(z,n)| = |a_0(z_0)| \exp\left[\left(jg_r - \frac{1}{2Q} + \frac{2g_r b}{g_i'}\right)n\right]$$

$$\exp\left[\frac{-2g_r z}{g_i'} + \frac{2jg_r b^{1/2}\sigma_z}{(jg_i')^{3/2}}\tan(q)\right] \left|\frac{\cos\left[\tan^{-1}\left(\left(\frac{jg_i z^2}{b\sigma_z^2}\right)^{1/2}\right)\right]}{\cos(q)}\right|^{2h_r/g_i'} \quad (4\text{-}24)$$

and the optical phase

$$\phi = \phi_0 + jg_i n - 2jg_i\sigma_z\left(\frac{b^{1/2}}{(jg_i')^{3/2}}\right)\left[\left(\frac{jg_i}{b}\right)^{1/2}\frac{z}{\sigma_z} - \frac{n}{\sigma_z}(bjg_i')^{1/2} - \tan(q)\right]$$

$$+\frac{2h_r}{g_i'}\ln\left|\frac{\cos(q)}{\cos\left[\tan^{-1}\left(\left(jg_i'z^2/b\sigma_z^2\right)^{1/2}\right)\right]}\right| \quad (4\text{-}25)$$

where $z_0 = \left(\sigma_z^2 b / jg_i'\right)^{1/2}\tan(q)$, and q is redefined as

$$q = \tan^{-1}\left(\left(\frac{jg_i'z^2}{\sigma_z^2 b}\right)^{1/2}\right) - \frac{n}{\sigma_e}(bjg_i')^{1/2}.$$

In the second case, where gain dominates desynchronism, $d \leq \frac{1}{2}jg_i'$ and the optical pulse tends to shift backward, equations (4-10) through (4-13) yield

$$s = \frac{\sigma_z}{2\sqrt{(-b)jg_i'}}\ln\left|\frac{b + \dfrac{z(s,z_0)\sqrt{(-b)jg_i'}}{\sigma_z}}{b - \dfrac{z(s,z_0)\sqrt{(-b)jg_i'}}{\sigma_z}}\right| - \frac{\sigma_z}{2\sqrt{(-b)jg_i'}}\ln\left|\frac{b + \dfrac{z_0\sqrt{(-b)jg_i'}}{\sigma_z}}{b - \dfrac{z_0\sqrt{(-b)jg_i'}}{\sigma_z}}\right|, \quad (4\text{-}26)$$

$$n(s,z_0) = s, \quad (4\text{-}27)$$

$$\left|a(s,z_0)\right| = \left|a_0(z_0)\right| exp\left[\left(jg_r - \frac{1}{2Q} + \frac{2g_r b}{g_i'} - 2jh_i\left(\frac{-b}{\sigma_z^2 jg_i'}\right)^{1/2}\right)s\right]$$

$$exp\left[\pm\left(-4g_r\sigma_z\left(\frac{-b}{jg_i'^3}\right)^{1/2}\left(\frac{1}{r\pm 1} - \frac{1}{re^{-w}\pm 1}\right)\right)\right]\left|\frac{r\pm 1}{re^{-w}\pm 1}\right|^{2h_i/g_i} \qquad (4\text{-}28)$$

$$\phi(s,z_0) = \phi_0(z_0) + jg_i s + \frac{2g_i sb}{g_i'} \pm \left[-4g_i\sigma_z\left(\frac{-b}{jg_i'^3}\right)^{1/2}\left(\frac{1}{r\pm 1} - \frac{1}{re^{-w}\pm 1}\right)\right]$$

$$-\left(\frac{2jh_r s}{\sigma_z}\right)\left(\frac{-b}{jg_i'}\right)^{1/2} \pm \frac{2h_r}{g_i'}\left(w + ln\left|\frac{re^{-w}\pm 1}{r\pm 1}\right|\right) \qquad (4\text{-}29)$$

where $w = 2s\big((-b)(jg_i')\big)^{1/2} / \sigma_z$.

Substituting equations (4-26) and (4-27) into equations (4-28) and (4-29) and redefining $w = 2n\big((-b)(jg_i')\big)^{1/2} / \sigma_z$ yields the optical amplitude

$$\left|a(z,n)\right| = \left|a_0(z_0)\right| exp\left[\left(jg_r - \frac{1}{2Q} + \frac{2g_r b}{g_i'} - 2jh_i\left(\frac{-b}{\sigma_z^2 jg_i'}\right)^{1/2}\right)n\right]$$

$$exp\left[\pm\left(-4g_r\sigma_z\left(\frac{-b}{jg_i'^3}\right)^{1/2}\left(\frac{1}{r\pm 1} - \frac{1}{re^{-w}\pm 1}\right)\right)\right]\left|\frac{r\pm 1}{re^{-w}\pm 1}\right|^{2h_i/g_i} \qquad (4\text{-}30)$$

and the optical phase

41

$$\phi = \phi_0(z_0) + jg_i n + \frac{2g_i nb}{g_i'} \pm \left[-4g_i \sigma_z \left(\frac{-b}{jg_i'^3} \right)^{1/2} \left(\frac{1}{r \pm 1} - \frac{1}{re^{-w} \pm 1} \right) \right]$$

$$- \left(\frac{2jh_r n}{\sigma_z} \right) \left(\frac{-b}{jg_i'} \right)^{1/2} \pm \frac{2h_r}{g_i'} \left(\pm s + ln \left| \frac{re^{-w} \pm 1}{r \pm 1} \right| \right)$$

(4-31)

where
$$r = \left| \frac{b + \frac{z}{\sigma_z}\left(-bjg_i'\right)^{1/2}}{b - \frac{z}{\sigma_z}\left(-bjg_i'\right)^{1/2}} \right|, \text{ and } z_0 = \left[\frac{b\sigma_z}{\left(-bjg_i'\right)^{1/2}} \right] \left[\frac{re^{-w} \pm 1}{re^{-w} \mp 1} \right].$$

The upper sign is used when $|z| < -b\sigma_z / \left(-bjg_i'\right)^{1/2}$, and the lower sign is used when z is not between these limits but is within the limits of the electron pulse. Outside the limits of the electron pulse, the phase remains constant and the optical amplitude has the form

$$|a(z,n)| = \left(1 - 2(z - dn)^2 / \sigma_a^2\right) exp(-n/2Q)$$

(4-32)

where σ_a is the width of the optical pulse.

The expressions (4-24), (4-25), and (4-30) through (4-32), provide an analytical solution for an initially parabolic optical and electron pulse. Figure 4-2 shows the comparison of the analytical solution with the results of a numerical solution for the same conditions. The desynchronism is $d = 0.015$, the initial field amplitude $a_0 = 0.001$ for all z, the phase $\phi_0(z) = 0$ for all z, the electron pulse length is $\sigma_z = 10$ at phase velocity v_0^* for maximum gain, and $Q = 100$. The initially long optical pulse takes on the apparently Gaussian shape shown at the upper left after $n = 60$ passes.
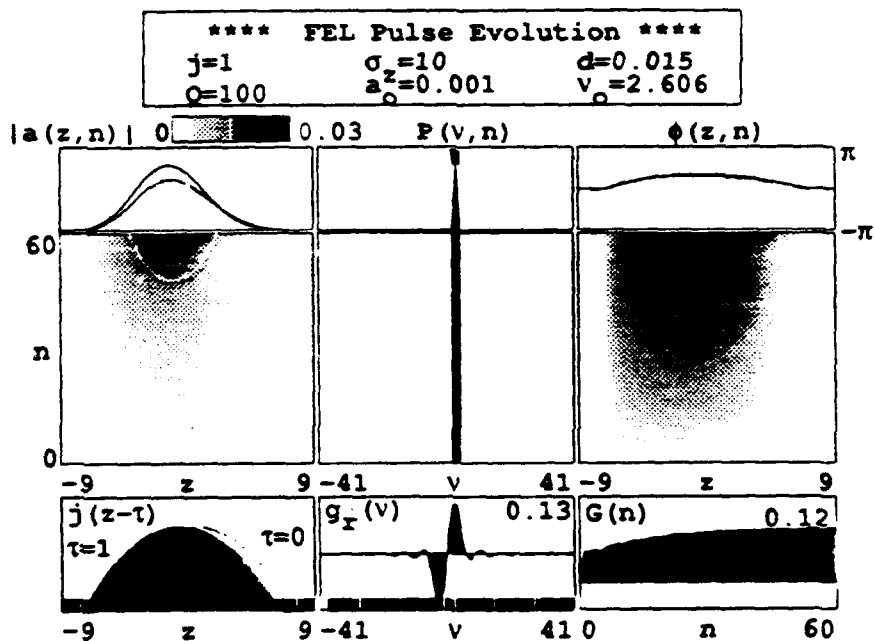
Figure 4-2. Optical pulse evolution comparing a numerical simulation with the analytical solutions for a parabolic electron pulse.

The analytical solution gives a slightly greater amplitude than the numerical simulation after $n = 60$ passes, but the shape and centroids of the pulses are nearly the same. The difference in amplitude is probably due to an accumulation of small numerical errors in the calculation of gain each pass. A difference in gains of only 0.3% over $n = 60$ passes would account for the discrepancy.

When $d = 0$, the second case is appropriate because $g_i'\left(v_0^*\right) > 0$ and equation (4-30) shows that the field $|a(z,n)| \rightarrow 0$ as $n \rightarrow \infty$. This situation is the well-known result that a pulsed FEL cannot operate at zero desynchronism [1]. Physically, the centroid of the optical pulse is shifting back over the electron pulse by an amount $\frac{1}{2} jg_i'$ for each pass through the undulator. Eventually there is no overlap between the pulses and the optical field decays to zero. Figure 4-3

43

shows a gain versus desynchronism curve for the parabolic electron pulse and initially constant optical pulse. The desynchronism for maximum gain is located at $d = \frac{1}{2} j g_i{}'$, which is the desynchronism necessary for the optical pulse centroid and electron pulse centroid alignment at the beginning of the undulator each pass.
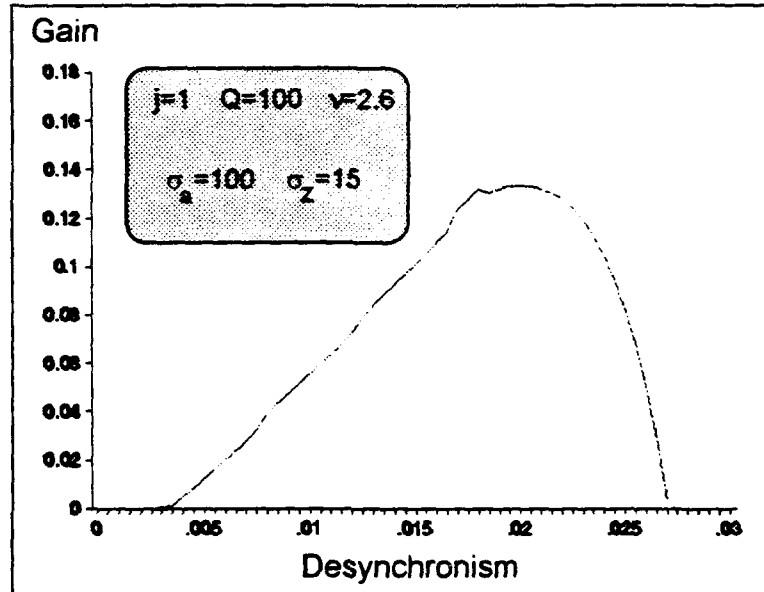

Figure 4-3. Gain vs. desynchronism for a parabolic electron pulse.

3. Triangular Electron Pulse

Another electron pulse shape that can be solved analytically using the method of characteristics with equations (4-8) and (4-9) is the triangular pulse shape of the form $\sigma(z) = 1 - |z| / \sigma_z$ with width σ_z for $|z| < \sigma_z$ and $\sigma(z) = 0$ otherwise. This case compares the differences in optical pulse shape and phase caused by the z^2 dependence of the parabolic electron beam with the z dependence of the triangular electron beam. Due to the discontinuity in the triangular pulse at its peak, $z = 0$, the solution has slight differences in form for $z < 0$ and $z > 0$. An error near $z = 0$ is to be expected, since the triangular pulse

44

shape violates the assumption that the electron pulse shape varies slowly; $\sigma'(z) << 1$. As in the parabolic case, the optical pulse slipping backward due to large desynchronism, $d > \frac{1}{2} jg_i'$, or forward due to predominant gain, $d > \frac{1}{2} jg_i'$, appears. However, the solutions to equations (4-8) and (4-9) for the triangular electron pulse shape do not lend themselves to being displayed in a form that makes these two cases obvious. Therefore, we shall solve for cases of $|z| \leq 2f\sigma_z / jg_i'$ and $|z| > 2f\sigma_z / jg_i'$.

Solving equations (4-10) through (4-13) for the first case of $|z| \leq 2f\sigma_z / jg_i'$ yields

$$z(s, z_0) = \frac{\mp 2\sigma_z}{jg_i'}\left[\left|-f + \frac{jg_i' z_0}{2\sigma_z}\right| \exp\left[\pm\left(\frac{jg_i' s}{2\sigma_z}\right)\right] - f\right] \quad , \quad (4\text{-}33)$$

$$n(s, z_0) = s \quad , \quad (4\text{-}34)$$

$$|a(s, z_0)| = |a_0(z_0)| \exp\left[\left(\frac{2g_r d}{g_i} - \frac{jh_i}{2\sigma_z} - \frac{1}{2Q}\right)s\right]$$

$$\times \exp\pm\left[\left(\frac{4g_r\sigma_z}{jg_i'^2}\right)\left|-f \pm \frac{jg_i' z}{2\sigma_z}\right|(1 - \exp-[jg_i's/(2\sigma_z)])\right] \quad , \quad (4\text{-}35)$$

$$\phi(s, z_0) = \phi_0(z_0) + \left(\frac{2g_i d}{g_i'} \pm \frac{jh_r}{2\sigma_z}\right)s$$

$$\pm\left[\left(\frac{4g_r\sigma_e}{jg_i'^2}\right)\left|-f \pm \frac{jg_i' z}{2\sigma_z}\right|\left(1 - \exp\left[\frac{-jg_i's}{2\sigma_z}\right]\right)\right] \quad , \quad (4\text{-}36)$$

where $f = \frac{1}{2} jg_i' - d$. Substituting equations (4-33) and (4-34) into equations (4-35) and (4-36) gives the optical amplitude

$$|a(z,n)| = |a_0(z_0)| \exp\left[\left(\frac{2g_r d}{g_i} - \frac{jh_i}{2\sigma_z} - \frac{1}{2Q}\right)n\right]$$

$$x \exp\pm\left[\left(\frac{4g_r\sigma_z}{jg_i'^2}\right)\left|-f \pm \frac{jg_i'z}{2\sigma_z}\right|\left(1 - \exp-\left[jg_i'n/(2\sigma_z)\right]\right)\right],$$ (4-37)

and optical phase

$$\phi(z,n) = \phi_0(z_0) + \left(\frac{2g_i d}{g_i'} \pm \frac{jh_r}{2\sigma_z}\right)n$$

$$\pm\left[\left(\frac{4g_r\sigma_z}{jg_i'^2}\right)\left|-f \pm \frac{jg_i'z}{2\sigma_z}\right|\left(1 - \exp\left[\frac{-jg_i'n}{2\sigma_z}\right]\right)\right].$$ (4-38)

The second set of analytical solutions are for $|z| > 2f\sigma_z / jg_i'$. Solving equations (4-10) through (4-13) for the case of $|z| > 2f\sigma_z / jg_i'$ gives

$$z(s,z_0) = \frac{\pm 2\sigma_z}{jg_i'}\left[\left|-f + \frac{jg_i'z_0}{2\sigma_z}\right|\exp\left[\pm\left(\frac{jg_i's}{2\sigma_z}\right)\right] + f\right],$$ (4-39)

$$n(s,z_0) = s \qquad ,$$ (4-40)

$$|a(s,z_0)| = |a_0(z_0)| \exp\left[\left(\frac{2g_r d}{g_i} - \frac{jh_i}{2\sigma_z} - \frac{1}{2Q}\right)s\right]$$

$$x \exp-\left[\left(\frac{4g_r\sigma_z}{jg_i'^2}\right)\left|-f \pm \frac{jg_i z}{2\sigma_z}\right|\left(1 - \exp-\left[jg_i's/(2\sigma_z)\right]\right)\right]$$ (4-41)

$$\phi(s,z_0) = \phi_0(z_0) + \left(\frac{2g_i d}{g_i'} \pm \frac{jh_r}{2\sigma_z}\right)s$$

$$-\left[\left(\frac{4g_r\sigma_z}{jg_i'^2}\right)\left|-f \pm \frac{jg_i'z}{2\sigma_z}\right|\left(1 - \exp\left[\frac{-jg_i's}{2\sigma_z}\right]\right)\right]$$ (4-42)

Substituting equations (4-39) and (4-40) into (4-41) and (4-42) gives the optical amplitude

$$|a(z,n)| = |a_0(z_0)| exp\left[\left(\frac{2g_r d}{g_i} - \frac{jh_i}{2\sigma_z} - \frac{1}{2Q}\right)n\right]$$

$$\times exp-\left[\left(\frac{4g_r\sigma_z}{jg_i'^2}\right)\left|-f \pm \frac{jg_i z}{2\sigma_z}\right|\left(1 - exp-\left[jg_i'n/(2\sigma_z)\right]\right)\right]$$

(4-43)

where $|a_0(z_0)|$ is the arbitrary initial optical pulse amplitude, and the optical phase

$$\phi(z,n) = \phi_0(z_0) + \left(\frac{2g_i d}{g_i'} \pm \frac{jh_r}{2\sigma_z}\right)n$$

$$-\left[\left(\frac{4g_r\sigma_z}{jg_i'^2}\right)\left|-f \pm \frac{jg_i'z}{2\sigma_z}\right|\left(1 - exp\left[\frac{-jg_i'n}{2\sigma_z}\right]\right)\right]$$

(4-44)

where $\phi_0(z_0)$ is the initial optical phase and

$$z_0 = \frac{2\sigma_z}{jg_i'}\left[\left(-f - \frac{jg_i'}{2\sigma_z}z\right)exp\left(\frac{jg_i'n}{2\sigma_z}\right) + f\right].$$

For both the amplitude and the phase solutions, the upper sign is used when $z > 0$ and the lower when $z < 0$.

The expressions (4-37), (4-38), (4-43) and (4-44) provide an analytical solution to the optical pulse amplitude, shape, and phase in the presence of a triangular electron pulse. Figure 4-4 shows a comparison of a numerical simulation and these analytical solutions for the same initial conditions. The desynchronism is $d = 0$, the initial field amplitude is $a_0 = 0.001$ for all z, the phase is $\phi_0(z) = 0$ for all z, the electron pulse length is $\sigma_z = 10$ at phase velocity v_0^* for maximum gain, and $Q = 100$. The lower-left panel shows the triangular electron pulse at the beginning of the undulator when $\tau = 0$, and at the end when $\tau = 1$, showing the slippage distance. The middle-left panel shows the optical

pulse evolution over $n = 40$ passes with the final pass displayed at the top-left. The analytical results are slightly larger in amplitude and more sharply peaked than the numerical simulation, but the centroid and shape correspond well. The middle-right panel shows the optical phase evolution over $n = 40$ passes with the final phase displayed at the top-right. As can be seen, there is excellent agreement between the analytical and numerical solutions.
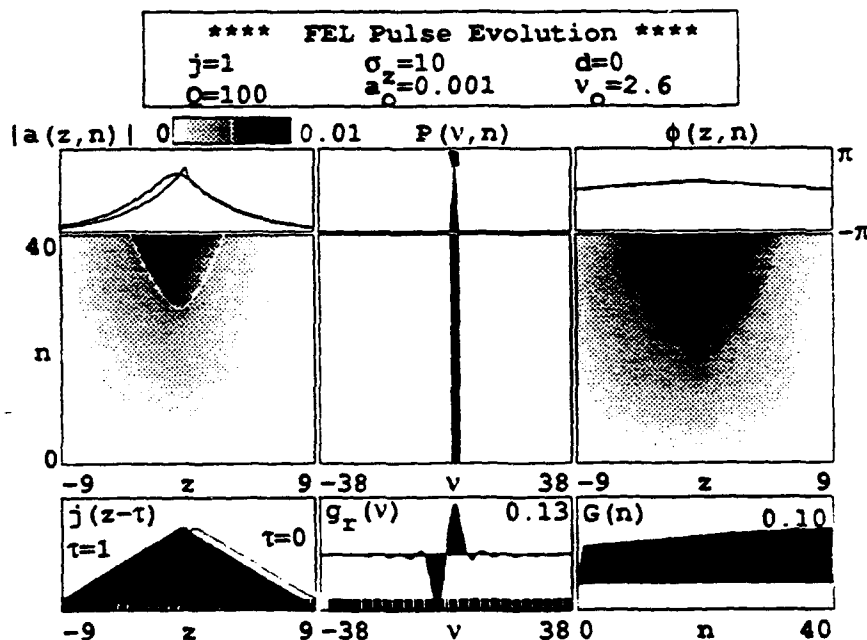

Figure 4-4. Optical pulse evolution comparing a numerical simulation with the analytical solutions for a triangular electron pulse.

D. COHERENCE DEVELOPMENT

The evolution of the optical amplitude and phase over many passes can be used to analytically examine coherence development. Taking the parabolic

electron beam with $d \leq \frac{1}{2} jg_i'$ as an example, the optical amplitude solution (4-30) on the first pass is given by $|a(z,n)| = |a_0(z_0)|$ where $|a_0(z_0)|$ represents an arbitrary optical pulse shape as a function of $z_0(z)$. After many passes, $n \to \infty$, the expression for z_0 becomes

$$z_0 = \frac{-b\sigma_z}{\left(-bjg_i'\right)^{1/2}} \qquad (4\text{-}45)$$

and the optical amplitude becomes

$$|a(z,n)| = |a(z_0)| \ exp\left[\left[\frac{2g_r d}{g_i'} - \frac{1}{2Q} - 2jh_i\left(\frac{\frac{1}{2}jg_i'-d}{\sigma_z^2 jg_i'}\right)^{1/2}\right]n\right]$$

$$\times exp\left[\pm\left[-4g_r\sigma_z\left(\frac{\frac{1}{2}jg_i-d}{jg_i'^3}\right)^{1/2}\left(\frac{1}{r(z)\pm1}\mp1\right)\right]\right]\left|r(z)+1\right|^{2h_i/g_i'} \qquad (4\text{-}46)$$

To obtain (4-46) from (4-30) we note that each term involving w as a negative exponent goes to zero since $w \to \infty$ as $n \to \infty$. Since z_0 is a constant after many passes, the first term in (4-46), which represents the effect of the initial optical pulse shape on the pulse shape after $n \to \infty$, has been reduced to a constant. This indicates that, after many passes, the optical pulse shape is not affected by the characteristics of the initial optical pulse. Therefore, this theory predicts that an initially random optical pulse evolves into the same shape as an initially smooth optical pulse. It follows that the theory should be applicable to FELs starting from classical spontaneous emission through coherence development to the onset of strong optical fields. It should be noted that the spontaneous, random field described here is classical, and does not involve the quantum processes analyzed in the previous section.

49

To observe the evolution of coherence development in a more quantitative way, several numerical solutions of equation (4-7) were obtained. Shown in Figure 4-5 is the coherence development of an initially random continuous wave optical field with average strength $a_0 = 1$, dimensionless current $j = 1.8$, initial phase velocity v_0^*, and parabolic electron pulse shape $\sigma(z) = 1 - 2z^2 / \sigma_z^2$ for $|z| < \sqrt{2}\sigma_z$ and zero for $|z| > \sqrt{2}\sigma_z$, of width σ_z with losses determined by $Q = 6$. The desynchronism is $d = 0.02$, and the initial optical amplitude has a random component added at each size z. The plot of $j(z - \tau)$ at the lower-left panel shows the parabolic electron pulse shape and the small slippage as τ goes from zero to one. The optical amplitude evolution $|a(z,n)|$ in the middle-left panel shows an initially random pulse which becomes much more coherent over $n = 40$ passes. The final pulse shape in the upper-left panel is much smoother and shows a high degree of coherence. The gain spectrum, $g_r(v)$ in the lower-center panel shows the antisymmetric gain function for reference. The evolution of the logarithm of the optical power spectrum, $\log\left(P(v,n)\right)$ is shown in the middle-center panel. The evolution of coherence leads to a spectrum centered at the phase velocity for maximum gain. The final power spectrum in the upper-center panel is narrow indicating long range phase coherence. The optical phase evolution $\phi(z,n)$ in the middle-right panel shows the development of the optical phase over $n = 40$ passes with the final phase profile at the upper-right. The power evolution $P(n)$ in the lower-right panel shows power initially decrease as incoherent parts of the optical field are removed by losses. Then the power begins to grow as the pulse becomes more coherent and more centered at the frequency for maximum gain. Figure 4-5 also implies that the optical shape is determined primarily by the shape of the electron pulse.
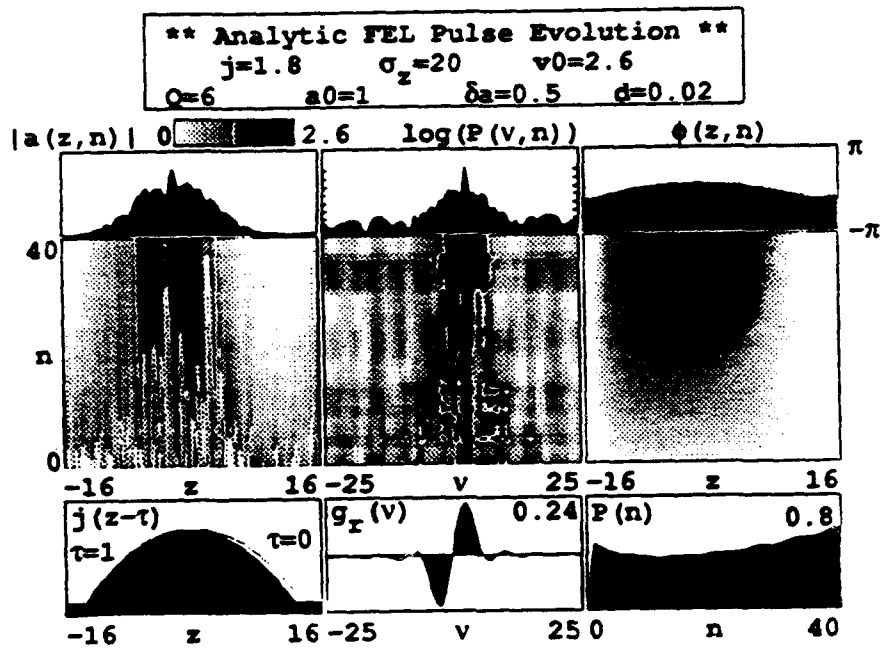
Figure 4-5. Optical coherence development from a random pulse solving (4-7) numerically.

E. CONCLUSIONS AND FURTHER RESEARCH SUGGESTIONS

By assuming a long electron pulse, weak optical fields, and low gain, the electron and optical pulse shapes have been expanded in a Taylor series in order to solve the pendulum and wave equations. The result is a single first-order, partial-differential equation describing the evolution of an optical pulse. By including the effects of desynchronism and resonator losses, a more complete partial-differential describes optical evolution over many passes in an FEL oscillator. As a direct consequence of deriving the differential equation, the familiar antisymmetric gain curve and symmetric optical phase shift are obtained, as well as functions describing the effects of slippage and the electron pulse shape. Solving the differential equation (4-7) for a continuous electron beam

51

yields the simple single-mode gain value of $0.135j$ and results in no change in the optical pulse shape. Electron pulses with parabolic and triangular shapes are shown to yield gains less than predicted by single-mode gain calculations since there are fewer electrons distributed over the entire length of the electron pulse. The shape of the electron pulse is shown to determine of the shape of the optical pulse in steady state after many passes. Coherence evolution of an initially random pulse is also studied.

V. SHORT PULSE EVOLUTION IN THE BOEING APLE OSCILLATOR

A. INTRODUCTION

The previous chapters have looked at FELs with low gain and weak optical fields. We now examine an FEL oscillator that can produce high gain and strong fields, but is designed to produce only moderate optical fields as a seed laser for an FEL amplifier. Indeed, the problem investigated is how to make an oscillator work poorly, or to reduce the electron-light coupling, so that only a small energy spread is induced in the electron beam. This chapter discusses the Boeing/LANL Average Power Laser Experiment (APLE) which is designed to produce 100 kW of average power for 3 minutes from a FEL using a Single Accelerator, Master Oscillator, Power Amplifier (SAMOPA) design, shown in Figure 5-1 [19,20].

1. Photo Injector
2. Accelerator Section
3. FEL Oscillator
4. Accelerator Section
5. Bunchers
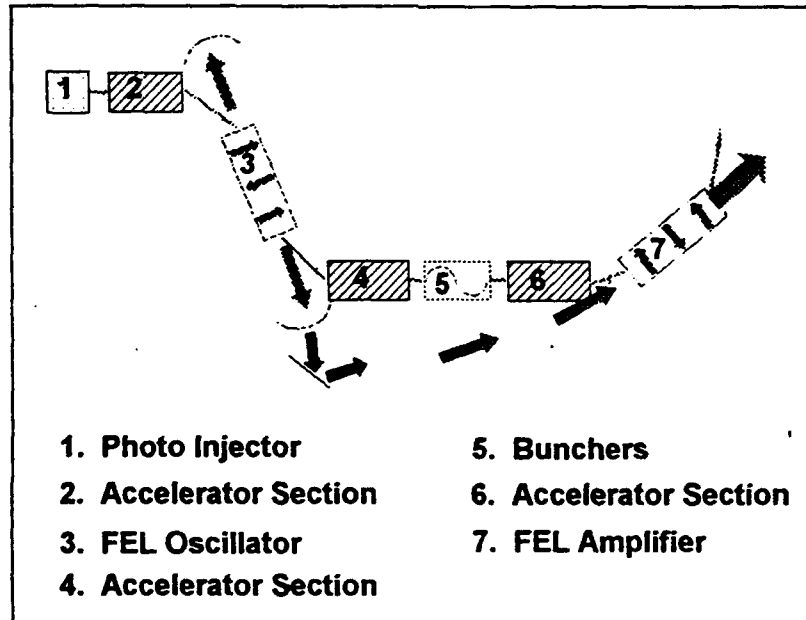6. Accelerator Section
7. FEL Amplifier

Figure 5-1. Schematic diagram of the Boeing APLE SAMOPA

In Figure 5-1, the accelerator section (2) preceding the FEL oscillator (3) gives the beam 17 MeV energy with an instantaneous energy spread of 0.3% at an average current of 0.23 A and a normalized emittance (90% edge) of $\varepsilon_n = 80\pi$ mm-mrad. The electron beam, with a peak current of 140 A is then directed into the oscillator (3) where it produces $\lambda = 10.6 \mu m$ wavelength radiation of approximately 100 W average power. Each electron micropulse may have an energy slew of up to 3% across the pulse. Emerging from the oscillator, the electron beam is accelerated (4), and then may be compressed in two interleaved bunchers (5) to increase peak current. The beam is then accelerated further (6) to 34 MeV and the energy slew removed. The electron beam enters the power amplifier (7) with a peak current of 450 A and an instantaneous energy spread of $\leq 1.0\%$. In the amplifier, the optical pulse from the oscillator experiences a gain of $G \approx 1000$ to meet the design criteria of 100 kW average laser power for 3 minutes [19,20].

This chapter examines the goal of passing an electron beam through the oscillator (3) without increasing its energy spread beyond $\approx 1.0\%$. This procedure produces an optical pulse with 100 W average power, and determines an optical pulse shape and size that optimizes the amplifier efficiency. The effect of an energy slew in the electron beam is investigated, and we also consider the optimum design for a high power oscillator.

B. OSCILLATOR DESCRIPTION

The APLE oscillator uses a linearly polarized undulator of wavelength $\lambda_0 = 2.36$ cm over $N = 100$ periods for a length of $L = N\lambda_0 = 2.36$ m and undulator parameter $K = e\bar{B}\lambda_0 / 2\pi mc^2 = 0.23$. The optical wavelength produced is determined from the resonance condition as

$\lambda = \lambda_0\left(1+K^2\right)/2\gamma^2 \approx 10.6\mu m$. The relatively large optical mode waist, $W_0 = 0.2\,cm$, compared to the small matched electron beam radius [1], $r_\bullet = \sqrt{\left(\varepsilon_n \lambda_0/2\pi K\right)} = 0.08$ cm, leads to an averaged filling factor of $F = \left(r_\bullet/W_0\right)^2/\left(1+L^2/12Z_0^2\right) \approx 0.12$ with Rayleigh length $Z_0 = L/2$. The electron beam density $\rho = 1.4 \times 10^{12}\,cm^{-3}$ gives a dimensionless current of $j = 8N\left(\pi eKLJJ\right)^2\rho/\gamma^3 mc^2 = 250$ where the Bessel function factor $JJ = J_0(\xi) - J_1(\xi) \approx 0.987$ with $\xi = K^2/2\left(1+K^2\right) \approx 0.025$ is present in order to account for the linearly polarized undulator [1]. The theoretical single-mode gain is estimated by $G = 0.135jF \approx 58\%$, but is not self consistent and does not include the effects of energy slew, beam quality, or optical mode distortion. The length of the electron micropulse is $l_\bullet = 1.8$ cm, or $\sigma_z \approx 17$ slippage distances, $N\lambda$.

The electron phase velocity, $v = L\left[\left(k + k_0\right)\beta_z - k\right]$, measures the resonance between the electron, undulator, and optical fields [1]. An electron beam energy spread causes a Gaussian spread in z velocities and phase velocities with standard deviation $\Delta v = \sigma_G = 4\pi N\Delta\gamma/\gamma \approx 1$ where $\Delta\gamma/\gamma = 0.0015$ for the APLE oscillator. A linear energy slew of 3% over the electron micropulse causes a ramp in phase velocities from $v \approx -25$ to $v \approx 25$. An angular spread of the beam causes an exponential spread in the phase velocity characterized by a $1/e$ width of $\Delta v_\theta = \sigma_\theta = 1.5$. The energy and angular spreads do not significantly degrade APLE oscillator performance. The large energy slew of $\Delta v \approx 50$ over $\sigma_z \approx 17$ slippage distances means that each slippage length of the beam experiences a phase velocity shift of $\Delta v \approx 3$ during each pass.

C. DIFFRACTION EFFECTS

When the effects of optical diffraction are included in the FEL interaction, the phase velocity for maximum gain is shifted by the Rayleigh length z_0 [1]. The electron phase velocity that gives the optimum peak single pass gain was found to be $v_0^{max} \approx 2.6 + 1/z_0 \approx 5$ [1]. Optical mode distortion results from high current which amplifies the radiation overlapping the electron beam. This effect causes the optical mode at the end of the undulator to decrease in size and increase the filling factor. A single pass, three dimensional, self-consistent numerical simulation including diffraction, electron beam radius, and beam quality was used to determine the electron phase velocity that produces the peak single-pass gain, v_0^{max}, and the new effective filling factor. The simulation used a peak current density of $j=250$, normalized electron beam radius $\sigma_\bullet = r_\bullet \sqrt{\pi/L\lambda} = 0.28$ with a parabolic shape [1], energy spread with standard deviation $\sigma_G = 1$ distributed as a Gaussian, angular spread described by an exponential distribution of $1/e$ width $\sigma_\theta = 1.5$, and a weak optical field.

The strong fields attained over many passes and the resonator mirrors can affect the steady-state distortion that occurs in steady-state. A multiple-pass numerical simulation including resonator mirrors and losses was next used to determine the optical mode distortion over multiple passes in strong optical fields. The losses were characterized by $Q = 5$, where $1/Q$ represents the fractional loss of optical power per pass in the resonator from both outcoupling and absorption. The resonator was characterized by a mirror radius so that the fundamental mode has edge loss around the mirrors of 1%. Strong optical fields cause the gain to decrease until the gain just equals the loss on each pass through the undulator. Since the gain is reduced, the amount of mode distortion is reduced. The effective filling factor now obtained by comparing the cross

sections of the undistorted optical mode with the distorted optical mode obtained from the multiple pass simulation gives $F \approx 0.04$. It is estimated that transverse diffraction and mode distortion in the FEL oscillator can be summarized by using an effective $jF \approx 10$ in two dimensional codes that explore longitudinal pulse effects.

D. PULSE EFFECTS

Running the APLE oscillator with a relatively large current of $jF = 10$, and extracting only 100W average power, while inducing less than 1% energy spread requires the electron-optical coupling to be significantly reduced. The first two cases presented below examine options for reducing the coupling. The last case increases the coupling to achieve high efficiency without the amplifier.

1. No Energy Slew in the Undulator

One method used to reduce electron - optical beam coupling is to operate at a large desynchronism, $d = -2\Delta S/N\lambda$, where ΔS is the mirror deviation from exact synchronism [1]. Small desynchronism values are known to cause unstable operation because a small change in resonator length can alter the FEL from high power to low power, or even zero power [1]. Figure 5-2 shows optical power versus desynchronism for the APLE oscillator. It was obtained using a two dimensional numerical simulation, including slippage effects with an electron pulse length of $\sigma_z \approx 17$, a Gaussian spread in electron phase velocities of $\sigma_G = 1.5$, and outcoupling and losses characterized by $Q = 5$.
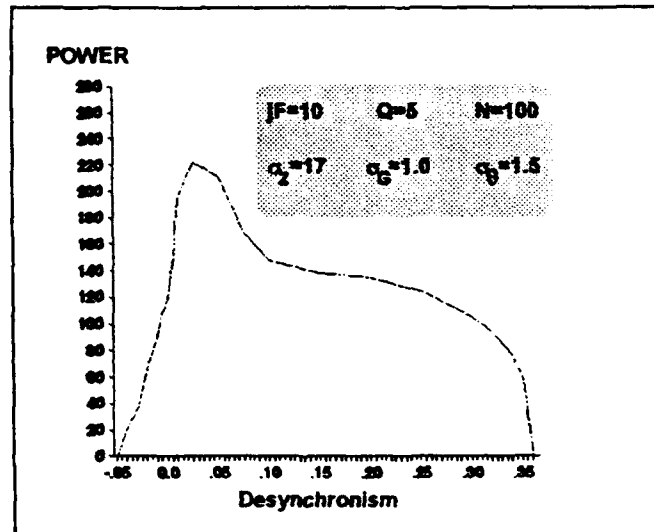
Figure 5-2. Power versus desynchronism for the APLE oscillator.

A larger, more optimum desynchronism of $d = 0.34$ gives low power, a long optical pulse, and a small induced energy spread, as shown in Figure 5-3. The long parabolic electron pulse of length $\sigma_z = 17$ is displayed in the lower-left panel showing the slippage over one pass through the undulator from dimensionless time $\tau = ct/L = 0$ to $\tau = 1$. The middle-left panel shows the optical pulse evolution growing from shot noise over $n = 800$ passes to a final peak optical amplitude of $|a| = 18$ shown at the top-left. The shot noise is introduced by including a random electron phase with standard deviation of $\delta\zeta = 10^{-5}$. The middle-center panel shows the evolution of the optical power spectrum over $n = 800$ passes with the top-middle panel displaying the final power spectrum. The bottom-center panel shows the single-mode gain spectrum for reference. The evolution of the electron distribution over the $n = 800$ passes is shown in the middle-right panel with the final distribution at the top-right. The bottom-right panel displays the evolution of the total optical power within the oscillator over $n = 800$ passes, with the final dimensionless power $P = 86$ corresponding to approximately 2200 W. Since the trailing half of the electron pulse never

interacts with the optical pulse, most of the energy distribution is kept within a narrow band. Only the electrons on the leading edge of the electron pulse give up energy to the light which produces the small bump on the left of the final electron distribution spectrum. The final energy spread is only about 0.6% and satisfies the APLE criteria.
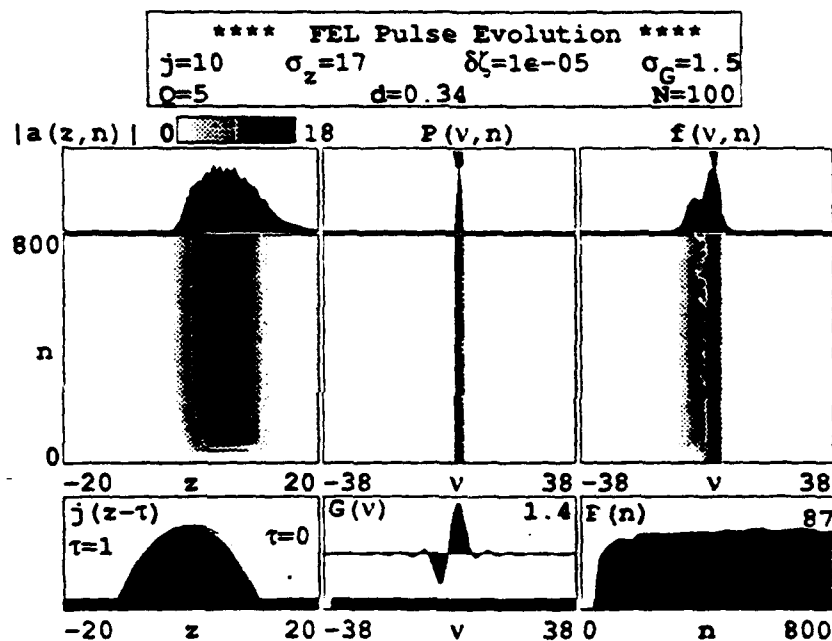
Figure 5-3. Optimum desynchronism of d=0.34 produces required power without inducing large energy spread.

The effects of a small random "jitter" in the electron energy coming from the accelerator was also explored. The study used the two-dimensional simulation but included a small random phase velocity component to each electron micropulse. A timing jitter was included by adding a small random change to the desynchronism length on each pass. These jitters had a

significant effect on small values of desynchronism and caused the FEL to not operate for the negative desynchronism values. This effect could be expected since the region of small desynchronism in Figure 5-2 is considered unstable. The jitters had little or no effect on the power at moderate to large desynchronism values.

2. Energy Slew in the Oscillator

Another option for the APLE SAMOPA design induces a linear electron energy slew of between 1% and 3% along the micropulse. The effect is to reduce electron-optical beam coupling in an attempt to leave large portions of each micropulse unaffected by interactions with the radiation field. The energy slew is converted to a slew in the electron phase velocities by $\Delta v = 4\pi N \Delta \gamma / \gamma$. The slew in phase velocities over a pulse length of $\sigma_z = 17$ slippage distances results in a shift of $\pi/4$ (1% slew) or $3\pi/4$ (3% slew) over each slippage distance. Superimposing a Gaussian energy spread of $\sigma_G = 1$ on the slewed pulse causes light to interact with electrons with phase velocity differences of $\approx \pi$. Since the change in phase velocity is greater than the gain bandwidth, the FEL interaction is affected. In order to reach a stable power and stable optical pulse shape when there is a significant energy slew, the desynchronism must be near zero so that the light continues to interact with the same energy component of each electron micropulse. Unfortunately, when the desynchronism is small, the FEL coupling is large resulting in strong optical fields and a large electron energy spread at the end of the interaction. A large desynchronism causes the light to experience a significant change in resonance condition as discussed above. In that case, a chaotic optical pulse shape and power evolution are observed in simulations.

Figure 5-4 shows the results of a two-dimensional multimode numerical simulation with $jF = 10$, a large desynchronism of $d = 0.06$, energy spread of $\sigma_G = 1.5$, and an energy slew of 3% over $n = 1500$ passes. The middle-left panel displays the chaotic optical pulse evolution with the final pulse shape shown at the top-left. The two upper-center panels show the broad optical power spectrum evolution due to a broad range of resonance conditions contained in the slewed electron pulse. The lower-right panel displays the chaotic power evolution in the resonator with about 50% power variations over a few hundred passes.
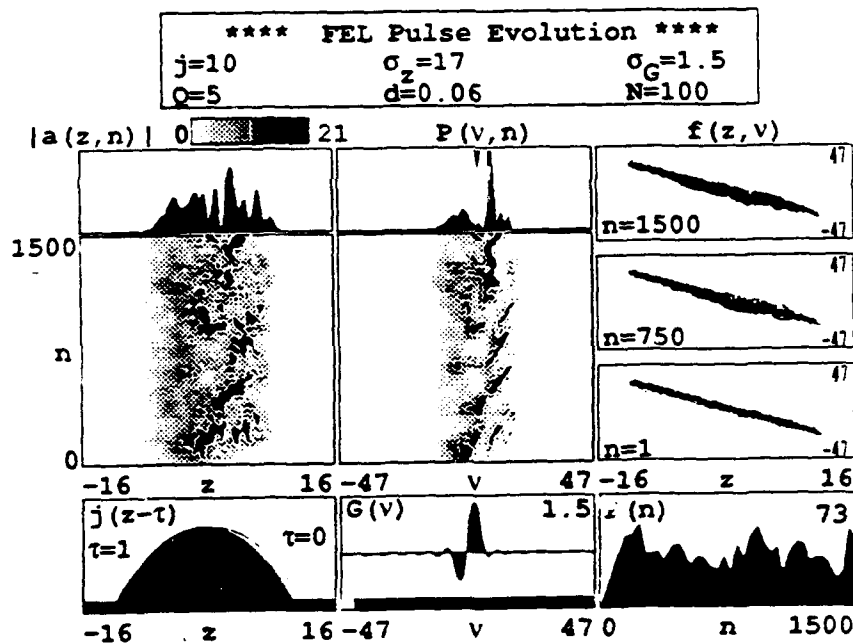

Figure 5-4. APLE oscillator with 3% linear electron energy slew present.

The three upper-right panels display the electron energy distribution as a phase velocity distribution at the end of passes $n = 1$, 750, and 1500. On the first pass, the 3% energy slew and the 0.3% Gaussian energy spread in the electron

61

micropulse are shown. In later passes, the electron-light interaction induces two to three times the energy spread originally present, which is the maximum allowable by APLE specifications.

3. High Power Oscillator Experiment

Another possible goal for the APLE laser system is the operation of the oscillator alone at the high average power of 10 kW for 3 minutes. This goal requires a complete change in design criteria and objectives from those of the previous two sections. Rather reducing the electron-optical beam coupling, the goal here is to increase coupling to get maximum power from the FEL oscillator.

The first method for increasing power simply increases the current density $j \propto K^2$ by increasing the undulator parameter K. This is accomplished by reducing the gap, g, between the undulator magnets, since $K \propto e^{-\pi g/\lambda_0}$. The increase in coupling is expressed by j occurs because increasing K will increase the transverse wiggling motion of the electrons; the amplitude of transverse oscillations is $\Delta x = K\lambda_0/2\pi\gamma$.

Secondly, the FEL power can be increased by using a small value of desynchronism as seen in Figure 5-2.

The two methods above increase FEL coupling and should lead to saturation in strong optical fields. Saturation occurs when a significant number of electrons have lost enough energy to move through the gain spectrum bandwidth $\Delta\gamma/\gamma \approx -1/2N$, which corresponds to a phase velocity change of $\Delta v = 4\pi N \Delta\gamma/\gamma \approx -2\pi$. Another view of the saturation process uses the FEL resonance condition $\lambda = \lambda_0(1+K^2)/2\gamma^2$. If a significant number of electrons lose enough energy, $(\gamma-1)mc^2$, the optical wavelength no longer remains in resonance with the electrons.

The resonance condition reveals several ways to go beyond the saturation point. As electrons lose energy along the undulator, the undulator's wavelength, λ_0, or the parameter, K, could be decreased so that resonance is maintained along the undulator. An undulator designed to take advantage of this concept is known as a "tapered undulator". Conceptually, reducing λ_0 or K provides a phase acceleration for the electrons with the effect of simply adding a phase velocity to the pendulum equation (2-14) describing the electrons' microscopic motion [1]:

$$\overset{\infty}{\zeta} = \overset{\circ}{v} = \delta + |a|\cos(\zeta + \phi), \qquad \text{where } \zeta = \int_0^\tau k_0(\tau')d\tau' + kz + \omega t, \quad (5\text{-}1)$$

where $k_0(\tau) = 2\pi/\lambda_0(\tau)$ is the changing undulator wavenumber along the undulator. Such tapering yields a phase acceleration of [1]

$$\delta = L^2 \frac{dk_0(z)}{dz}. \qquad (5\text{-}2)$$

In order to increase coupling, the undulator parameter is increased to $K = 0.8$. The three-dimensional numerical simulation using $K=0.8$ yields a new effective filling factor resulting in $jF = 70$. A small value of desynchronism $d = 0.001$ enhances electron-optical beam coupling further. The phase acceleration $\delta = 8\pi$ continues to extract energy from the electrons after saturation. Figure 5-5 displays the results of a two-dimensional numerical simulation using losses represented by $Q = 10$ over $n = 1000$ passes. The optical pulse is modulated by the trapped-particle instability and grows to a final peak amplitude of $|a| = 570$. The trapped-particle instability occurs when electrons trapped in phase space oscillate at the synchrotron frequency leading to the formation of several sidebands. The final average power $P = 2.5 \times 10^4$

corresponds to approximately 20 kW and is twice the high power goal of the oscillator.
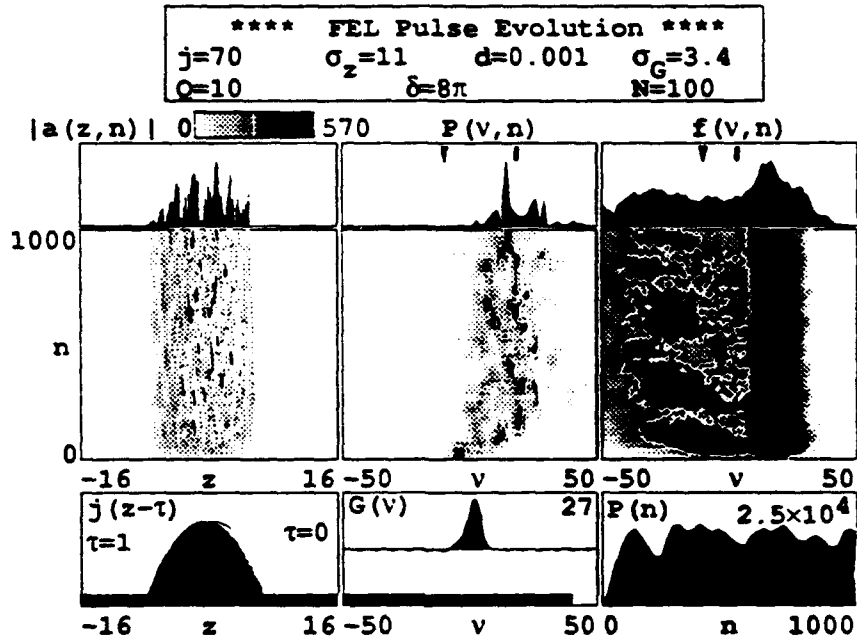
Figure 5-5. High average power from tapered oscillator.

E. CONCLUSIONS AND FURTHER RESEARCH SUGGESTIONS

The Boeing/LANL Average Power Laser Experiment (APLE) design required limiting the electron-optical coupling in the oscillator in order to reduce the energy spread of the electron pulse prior to injection into the amplifier. Several methods of limiting the coupling were examined, including the use of large desynchronisms and the use of an energy slew in the electron pulse. Large desynchronisms were found to meet the requirements of a smooth, relatively long optical pulse with less than double the initial energy spread of the electron pulse.

Using an energy slew to reduce electron-optical coupling resulted in a chaotic optical pulse and energy extraction from a large portion of the electron pulse.

Producing a high average power optical pulse using a tapered oscillator without the amplifier was examined in this chapter. Further investigation on the ability of the mirrors to withstand the high optical powers incident on them, or a proposal for a mirror system that can operate at those powers, is needed.

VI. WHISTLER WAVE AMPLIFICATION IN THE MAGNETOSPHERE

A. INTRODUCTION

1. Description of Whistler Waves

Whistler waves are very low frequency (VLF) electromagnetic radiation that propagates through the earth's ionosphere and magnetosphere, and are detected at magnetically conjugate field points on the earth's surface [21]. Whistler waves were first commonly detected during World War I by each side as they used amplifiers on long telephone lines to listen to the other's conversations [22]. Instead, what they sometimes heard were whistling sounds decreasing in frequency from several to one kHz over a period of about one second. The long telephone lines were acting as antennas for these whistlers, and the high gain devices boosted the otherwise weak signal. It also found that the rate of whistler activity varied with time of day, magnetic activity, and location on the earth [21]. Whistlers are more common at night, in mid-latitudes, and during periods of increased lightning activity [22].

The correlation between periods of high lightning activity and whistler detection led to the following explanation for their occurrence. A lightning flash in the southern hemisphere dumps electromagnetic energy into the atmosphere in a short broad-band pulse. This pulse may then propagate through the ionosphere and into the magnetosphere. The magnetosphere is highly dispersive, so as the pulse travels along a magnetic-field-aligned duct it is spread out due to higher frequencies traveling faster than lower ones. The wave may also be amplified as it propagates along the field line by interactions with

energetic charged particles. As the wave emerges from the magnetosphere at the conjugate point in the northern hemisphere, it is detected as a whistler beginning with higher frequencies and trailing off to lower frequencies.

Other mechanisms have also been found to generate whistler waves. Morse code dashes longer than 150 milliseconds may produce whistlers accidentally [22]. VLF transmitters placed in mid-latitudes may stimulate whistlers detected at the conjugate point. Over the last forty years, whistler waves have primarily been studied using VLF transmitters to simulate the injected whistler [22].

2. Description of the Magnetosphere

The immediate environment of the earth consists of a neutral atmosphere extending up to about 60 km above the earth's surface, the ionosphere, a region consisting of increasingly ionized gas as well as neutral particles extending up to about 1000 km in altitude, and the magnetosphere, consisting of ionized hydrogen and free electrons, extending out to distances of about 100,000 km from the earth [23]. There is no distinct boundary between the ionosphere and magnetosphere; it is rather a smooth continuum.

The structure and processes of the magnetosphere are controlled by the earth's magnetic field and the solar winds from the sun. The interaction of the solar wind and the earth's magnetic field forms the bow-shock at approximately $12R_e$ (where $R_e = 6370$ km is the mean radius of the earth) with the solar wind dragging field lines around the earth forming a tail on the anti-solar direction.

The region in space in which the earth's magnetic field is closely approximated by a centered dipole field inclined at $11°$ to the spin axis is known as the inner magnetosphere [23]. The inner magnetosphere extends out to about $7R_e$ and is populated by a background 'cold' plasma with energies of 0.1

67

to 1 eV and a less dense 'hot' plasma with energies from 1 keV to 100 MeV [23]. These energetic charged particles are magnetically trapped in helical orbits spiraling along field lines and make up the radiation belts. Figure 6-1 shows the inner magnetosphere with dipole magnetic field lines and the helical paths of energetic trapped particles. The cold plasma is responsible for the index of refraction for VLF while the part of the hot plasma that is resonant with the VLF wave can amplify the wave. A typical value for the index of refraction is n ≈ 20 to 30 due to the cold plasma.
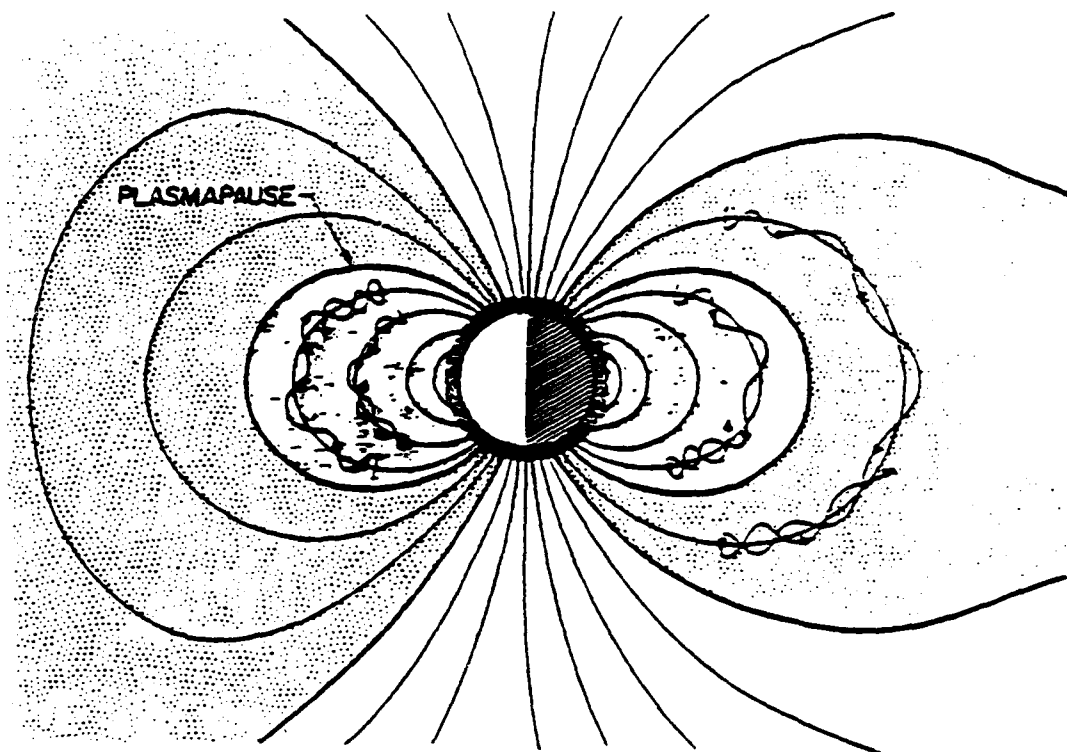

Figure 6-1. Inner magnetosphere with dipole field lines and energetic particle paths.

Approximating the earth's magnetic field as a centered dipole inclined by 11° from the axis of rotation yields the following equation for the magnetic field:

$$B(R, \Lambda) = B_0 \left(\frac{R_e}{R} \right)^3 \sqrt{(1 + sin^2 \Lambda)}, \qquad (6\text{-}1)$$

where B_0 is the magnetic field at the surface of the earth, R is the geocentric distance to the field line, and Λ is the geomagnetic latitude [23]. A dipole field line can be described by

$$R = R_{eq} cos^2 \Lambda, \qquad (6\text{-}2)$$

where R_{eq} is the geocentric distance to the field line at the equator [23]. Field lines are uniquely identified by the L parameter

$$L = \frac{R_{eq}}{R}. \qquad (6\text{-}3)$$

The term "ducting" is used to describe the bending of the wave as it travels up along a field line in the southern hemisphere and back down the field line in the northern hemisphere. Ducts consisting of crests of higher electron density, or troughs of lower electron density, have been found to exist along field lines in the magnetosphere [22]. The electron density gradient creates an index of refraction gradient within a duct that causes a wave initially entering a duct to become trapped much like light in an optical fiber. Since the wave is traveling from a higher to a lower index of refraction, a form of total internal reflection may take place under the right initial conditions.

B. WAVE PARTICLE INTERACTIONS

1. The Cold Background Plasma

VLF waves propagating through the magnetosphere are affected by the hot and cold plasma in the region of interaction. The electrons in the cold plasma are several orders of magnitude less energetic than the electrons in the

69

hot plasma and are not resonant with the VLF wave. The only effect of the cold plasma on the VLF wave is to cause dispersion. The cold particle density ρ_c is several orders of magnitude greater than the density of the hot particles.

Since the VLF wave travels along a magnetic field line, a useful coordinate system near the geomagnetic equator has the z-axis follow a field line, as seen in Figure 6-2.
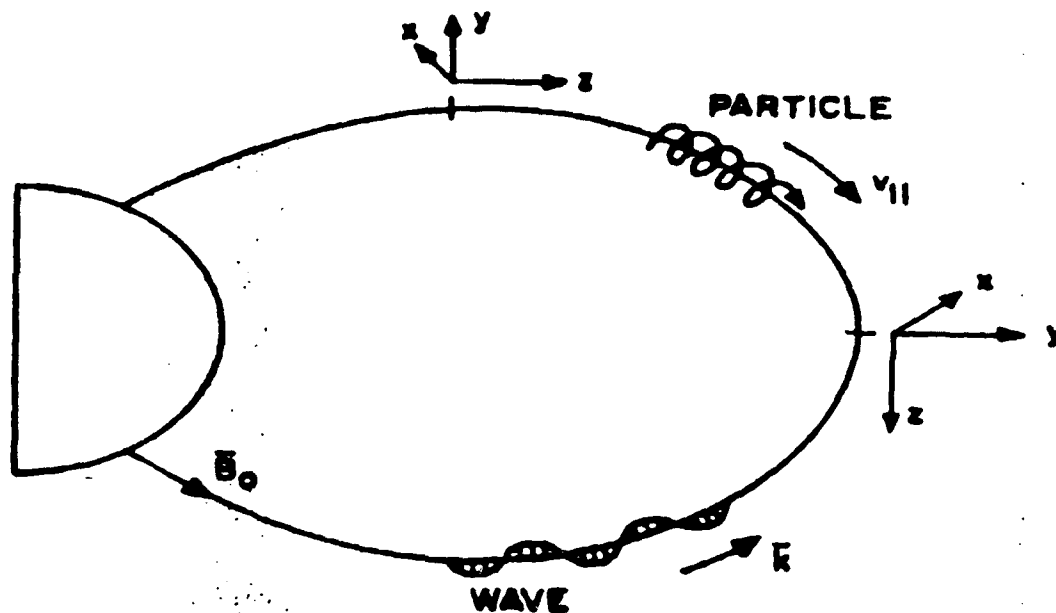
Figure 6-2. A field line showing the direction of propagation of the wave and electrons and a relevant coordinate system.

The cold particles' motion is governed by the Lorentz force law

$$m\dot{\bar{v}} = q\left(\bar{E}_w + \frac{\bar{v}}{c}\left(\bar{B}_w + \bar{B}\right) \right)$$ (6-4)

where $(\dot{..}) = d(..)/dt$, q is the charge on the particle, $\bar{E}_w = E_x\hat{x} + E_y\hat{y}$ is the VLF's arbitrary electric field, $\bar{B}_w$ is the VLF's arbitrary magnetic field, $\bar{B} = B_0\hat{z}$ is the

70

earth's magnetic field, and $\bar{v}$ is the velocity of the particle. Since the free ions are much more massive than the free electrons, they can be considered as being immobile at VLF driving frequencies. Assuming the wave oscillates at frequency ω, the linearized equation (6-4) yields

$$-im\omega v_y = -e\left(E_y - \frac{v_x}{c}B_0\right), \qquad (6\text{-}5)$$

and

$$-im\omega v_x = -e\left(E_x + \frac{v_y}{c}B_0\right), \qquad (6\text{-}6)$$

the VLF wave magnetic field has been dropped since it is always measured to be much less than the earth's magnetic field [21]. Solving equations (6-5) and (6-6) algebraically for the cold electron velocity, we find

$$v_x = \frac{e}{m\omega}\left(iE_x - \frac{\Omega}{\omega}E_y\right)\left(1 - \frac{\Omega^2}{\omega^2}\right)^{-1}, \qquad (6\text{-}7)$$

and

$$v_y = \frac{e}{m\omega}\left(iE_y + \frac{\Omega}{\omega}E_x\right)\left(1 - \frac{\Omega^2}{\omega^2}\right)^{-1}, \qquad (6\text{-}8)$$

where $\Omega = eB_0/mc$ is the electron gyro-frequency.

The Lorentz force law shows how the VLF wave affects the motion of the cold electrons. The wave equation is required to see how the cold electrons affect the wave. Ampere's law and Faraday's law are

$$\bar{\nabla} \times \bar{B}_w = \frac{4\pi}{c}\bar{J}_c + \frac{1}{c}\frac{\partial \bar{E}_w}{\partial t}, \qquad (6\text{-}9)$$

$$\bar{\nabla} \times \bar{E}_w = -\frac{1}{c}\frac{\partial \bar{B}_w}{\partial t}, \qquad (6\text{-}10)$$

71

and result in the wave equation

$$-\vec{k}\left(\vec{k}\cdot\vec{E}_w\right) + k^2\vec{E}_w = \frac{i4\pi\omega}{c^2}\vec{J}_c + \frac{\omega^2}{c^2}\vec{E}_w, \tag{6-11}$$

where $\vec{J}_c = -e\rho_c\vec{v}$ is the cold electron current density. Substituting the cold electron velocity equations (6-7) and (6-8) into the wave equation (6-11) yields

$$\left(\omega^2 - c^2k^2\right)E_y = \frac{\omega_{pc}^2}{1-\Omega^2/\omega^2}\left(E_y + i\frac{\Omega}{\omega}E_x\right), \tag{6-12}$$

and

$$\left(\omega^2 - c^2k^2\right)E_x = \frac{\omega_{pc}^2}{1-\Omega^2/\omega^2}\left(E_x - i\frac{\Omega}{\omega}E_y\right), \tag{6-13}$$

where $\omega_{pc}^2 = 4\pi e^2\rho_c/m$ is the cold electron plasma frequency. Solving equations (6-12) and (6-13) simultaneously then yields the dispersion equation relating k and ω. From the dispersion equation may be obtained the index of refraction caused by the cold electrons,

$$n^2 = \frac{c^2k^2}{\omega^2} = 1 - \frac{\omega_{pc}^2}{\omega(\omega \pm \Omega)}. \tag{6-14}$$

The plus sign corresponds to the index of refraction for a left-hand circularly-polarized wave; the minus sign corresponds to a right-hand circularly-polarized wave. The whistler wave has a frequency less than the electron gyro-frequency, and must be a right-hand circularly-polarized wave.

2. The Whistler Wave Equation

Having developed the index of refraction, which is interpreted as the effect of the cold electrons on the whistler wave, the effect of the hot electrons on the whistler wave is now explored. Referring back to Maxwell's equations used in the last section, the current density must now include the hot electrons

72

also: $\bar{J} = \bar{J}_h + \bar{J}_c$, where $\bar{J}_h = -ev_{h\perp}[-\sin\Theta, \cos\Theta, 0]$ is the single particle current density and $\Theta = \int_0^t \Omega(t')dt'$ is the phase of the electron cyclotron motion. When the wave envelope is a narrow band whistler, the slowly varying amplitude and phase approximations may be used in Maxwell's equations, $\partial_t E_w << \omega E_w$, $\partial_z E_w << kE_w$, $\partial_t \phi << \omega\phi$, $\partial_z \phi << k\phi$, where $\partial_z = \partial(..)/\partial z$ and $\partial_t = \partial(..)/\partial t$ [1].

Having shown in the last section that whistler waves are right-hand circularly-polarized, the fields can be expressed as

$$\bar{E}_w = E_w[\cos\psi, -\sin\psi, 0], \quad \bar{B}_w = B_w[\sin\psi, \cos\psi, 0], \qquad (6\text{-}15)$$

where $\psi = kz - \omega t + \phi$. Inserting the whistler fields into Ampere's law while allowing the amplitude and phase to evolve results in the following equation:

$$\partial_z B_w[-\cos\psi, \sin\psi, 0] + B_w(k + \partial_z\phi)[\sin\psi, \cos\psi, 0] - \frac{1}{c}\partial_t E_w[\cos\psi, \sin\psi, 0] + \frac{E_w}{c}(-\omega + \partial_t\phi)[\sin\psi, \cos\psi, 0] = \frac{4\pi}{c}\bar{J}. \qquad (6\text{-}16)$$

Defining the two orthogonal unit vectors

$$\hat{\varepsilon}_1 = [\sin\psi, \cos\psi, 0] \quad \text{and} \quad \hat{\varepsilon}_2 = [\cos\psi, -\sin\psi, 0] \qquad (6\text{-}17)$$

and projecting equation (6-16) onto them yields the following two scalar, first-order differential equations:

$$cB_w\partial_z\phi + E_w\partial_t\phi + ckB_w - \omega E_w = \frac{\omega_{pc}^2 E_w}{\Omega - \omega} - 4\pi ev_{h\perp}\cos(\psi + \Theta), \qquad (6\text{-}18)$$

and

$$c\partial_z B_w + \partial_t E_w = -4\pi ev_{h\perp}\sin(\psi + \Theta). \qquad (6\text{-}19)$$

These equations can be further simplified by using the index of refraction equation (6-14) and $nE_w = B_w$ to obtain

$$nc\partial_z B_z + \partial_t B_z = -4\pi env_{h\perp}\sin(\psi + \Theta),\qquad(6\text{-}20)$$

and

$$B_w(nc\partial_z\phi + \partial_t\phi) = -4\pi env_{h\perp}\cos(\psi + \Theta).\qquad(6\text{-}21)$$

We next define a complex whistler field b as

$$b = \frac{eB_w}{mc}e^{i\phi}.\qquad(6\text{-}22)$$

Then equations (6-20) and (6-21) further simplify to

$$\left(nc\frac{\partial}{\partial z} + \frac{\partial}{\partial t}\right)b = \frac{i4\pi e^2}{m}v\,exp(-i(\zeta+\Theta)),\qquad(6\text{-}23)$$

where $v = nv_{h\perp}/c$ is the normalized hot electron transverse velocity and

$$\zeta = kz - \omega t + \int_0^t \Omega(t')dt'$$

is the longitudinal electron phase.

The single-particle current for the hot electron in equation (6-23) is transformed into a beam of electrons by a weighted average over their transverse velocities v, their transverse phases Θ, and their longitudinal phase ζ. The averaging is weighted by the hot electron density ρ_h. We also can assume the whistler wave is spatially flat over many wavelengths [26] so that $\partial b/\partial z \approx 0$ to obtain the whistler wave equation

$$\dot{b} = -i\omega_{ph}^2\langle v\cdot exp(-i(\zeta+\Theta))\rangle.\qquad(6\text{-}24)$$

A whistler wave entering the magnetosphere encounters many electrons randomly spread in phase. As the whistler wave equation (6-24) shows, the interaction with randomly spread electrons has no effect on the whistler and the wave does not grow. However, the whistler wave affects the motion of the hot electrons. It is this feedback mechanism that allows electron bunching and wave

amplification. The effect of the wave on the motion of the electrons is the next topic to be examined.

3. The Hot Electron Equations of Motion

The motion of the hot electrons in the presence of the earth's magnetic field and the whistler wave fields is governed by the Lorentz force law

$$\dot{\bar{v}}_h = -\frac{e}{m}\left[\bar{E}_w + \frac{\bar{v}_h}{c} \times \left(\bar{B}_w + \bar{B}\right)\right]. \tag{6-25}$$

However, unlike the cold electron case, the whistler magnetic field is retained to describe electron bunching. Since the contributions of the cold electrons has been completely contained in the dispersion relation (6-14), the subscripts "h" for hot and "c" for cold are now dropped after 6-25.

The microscopic bunching of the electrons due to the wave-particle interaction is a small perturbation on the macroscopic gyro-motion and the bounce motion of the electrons in the earth's magnetic field. The earth's field near the geomagnetic equator is not exactly uniform, because the dipole's magnetic field lines diverge as they leave the north pole and converge as they enter the south pole. This results in a component of the field in the radial direction $\hat{r}$, as well as in the previously defined $\hat{z}$ direction [24]. In order to find the effect of the radial component B_r of the earth's magnetic field on the motion of the electrons, Maxwell's equation $\bar{\nabla}\cdot\bar{B} = 0$ is used to find B_r:

$$\frac{1}{r}\frac{\partial}{\partial r}\left(rB_r\right) + \frac{\partial B_z}{\partial z} = 0 \tag{6-26}$$

which gives

$$B_r = \frac{1}{2}r\left(\frac{\partial B_z}{\partial z}\right)_{r=0}. \tag{6-27}$$

The Lorentz force in the $\hat{z}$ direction due to this field is

$$m\dot{v}_z = -\tfrac{1}{2}\frac{ev_\perp r}{c}\frac{\partial B_z}{\partial z} \qquad , \qquad (6\text{-}28)$$

where $v_\perp$ is the hot electron's gyro-velocity. Averaging over one gyration and identifying $r = mv_\perp c/eB$ as the Lamor radius of gyration yields [24]

$$\dot{v}_z = -\frac{v_\perp^2}{2B_z}\frac{\partial B_z}{\partial z}. \qquad (6\text{-}29)$$

Since the electron energy is roughly constant while spiraling along field lines $(v_z^2 + v_\perp^2 = \text{constant})$, we have $v_z\dot{v}_z \approx -v_\perp\dot{v}_\perp$, so that

$$\dot{v}_x = \frac{v_x v_z}{2B_z}\frac{\partial B_z}{\partial z}, \qquad (6\text{-}30)$$

and

$$\dot{v}_y = \frac{v_y v_z}{2B_z}\frac{\partial B_z}{\partial z}. \qquad (6\text{-}31)$$

Recognizing $v_\perp^2/(2B_z)$ in equation (6-29) as a form of the first adiabatic invariant [24], it is therefore a constant. Thus equation (6-29) can be written in terms of the values of the initial transverse velocity $v_{\perp 0}$ and magnetic field, B_0, at the equator.

Adding equations (6-29), (6-30) and (6-31) into (6-25) gives the hot electron's equation of motion including the effects of the whistler wave and the earth's inhomogeneous magnetic field. Expressing each velocity component yields

$$\dot{v}_x = -\frac{e}{m}\left[E_x + \frac{1}{c}\left(v_y B_z - v_z B_y\right)\right] + \frac{v_x v_{z_c}}{2B_z}\frac{\partial B_z}{\partial z}, \qquad (6\text{-}32)$$

$$\dot{v}_y = -\frac{e}{m}\left[E_y + \frac{1}{c}(v_z B_x - v_x B_z)\right] + \frac{v_y v_{z_0}}{2B_z}\frac{\partial B_z}{\partial z}, \qquad (6\text{-}33)$$

$$\dot{v}_z = -\frac{e}{mc}\left(v_x B_y - v_y B_x\right) - \frac{v_{\perp 0}^2}{2B_0}\frac{\partial B_z}{\partial z}. \qquad (6\text{-}34)$$

Since the region of space most often identified with the whistler wave-particle interaction is within a few degrees of the geomagnetic equator, a useful approximation to the earth's dipole magnetic field in that region is

$$B_z = B(z) = B_0\left(1 - qz^2\right), \qquad (6\text{-}35)$$

where $q = 9/\left(2L^2 R_e^2\right)$, B_0 is the magnitude of the earth's magnetic field on the field line at the equator, and z is distance measured along a field line from the equator [25].

Substituting the form in equation (6-35), for B_z as well as for B_x and B_y and the right-handed circularly-polarized whistler wave from equation (6-15) into equations (6-32), (6-33), and (6-34) yields

$$\dot{v}_x = -\frac{e}{m}\left(E\cos\psi + \frac{v_y}{c}B(z) - \frac{v_z}{c}nE\cos\psi\right) + v_x v_{z_0}qz, \qquad (6\text{-}36)$$

$$\dot{v}_y = -\frac{e}{m}\left(-E\sin\psi - \frac{v_x}{c}B(z) - \frac{v_z}{c}nE\sin\psi\right) + v_y v_{z_0}qz, \qquad (6\text{-}37)$$

$$\dot{v}_z = -\frac{e}{m}\left(\frac{v_x}{c}nE\cos\psi - \frac{v_y}{c}nE\sin\psi\right) - \left(v_{\perp_0}^2\right)qz. \qquad (6\text{-}38)$$

These equations can be further simplified in terms of the perpendicular velocity $v_\perp$ and the angle Θ between the whistler wave fields and the electron's velocity,

$$v_y = v_\perp \cos\Theta, \qquad v_x = -v_\perp \sin\Theta. \qquad (6\text{-}39)$$

where $\Theta = \theta + \int_0^t \Omega(t')dt'$. After some algebra, the equations of motion reduce to

$$\dot{v}_z = -v_{\perp_0}^2 qz + \frac{eB_w v_\perp}{mc} \sin(\psi + \Theta), \qquad (6\text{-}40)$$

$$\dot{v}_\perp = v_{z_0} v_\perp qz + \frac{eB_w}{nm}\left(1 - \frac{nv_z}{c}\right)\sin(\psi + \Theta), \qquad (6\text{-}41)$$

$$\dot{\Theta} = \frac{eB(z)}{mc} + \frac{eB_w}{nmv_\perp}\left(1 - \frac{nv_z}{c}\right)\cos(\psi + \Theta). \qquad (6\text{-}42)$$

Introducing the whistler wave amplitude $|b| = eB_w/mc$ and the electron gyro-frequency $\Omega = eB(z)/mc$ yields

$$\dot{v}_z = -v_{\perp_0}^2 qz + |b|v_\perp \sin(\psi + \Theta), \qquad (6\text{-}43)$$

$$\dot{v}_\perp = v_z v_\perp qz + \frac{c|b|}{n}\left(1 - \frac{nv_{z_0}}{c}\right)\sin(\psi + \Theta), \qquad (6\text{-}44)$$

$$\dot{\Theta} = \Omega(z) + \frac{c|b|}{nv_\perp}\left(1 - \frac{nv_{z_0}}{c}\right)\cos(\psi + \Theta). \qquad (6\text{-}45)$$

The first terms on the right side of each equation (6-43) through (6-45) describe the fast macroscopic electron motion in the large scale dipole field of the earth. The last terms are proportional to the VLF wave field $|b|$ and describe the small microscopic scale motion in the combined dipole and VLF fields.

Since the hot electrons spend much less time in the interaction region than the bounce period in the dipole field, the electron motion in the first term on the right side of equations (6-43) through (6-45) can be described by

$$z_{macro}(t) \approx v_{z_0} t. \qquad (6\text{-}46)$$

78

According to experimental observations, most whistler activity and VLF wave amplification occurs when $\omega = 0.5\Omega$, known as the "cutoff frequency" [22]. At the cutoff frequency, the phase and group velocities of the wave are given by $v_p = c/n$ and $v_g = d\omega/dk = c/n$ respectively. Since at resonance $v \approx 0$, the electrons satisfy $kv_{z_0} = \omega - \Omega$ so that $v_{z_0} = -\omega/k = -v_p = -c/n$. Hence, the wave at the cutoff frequency and the resonant electrons are traveling with equal velocities in opposite directions.

Recognizing that Θ has both fast and a slowly rotating terms allows us to separate out the simple, fast periodic gyro-motion of the electrons in order to concentrate on the more interesting slower evolution of the bunching electrons. Redefining $\Theta = \theta_f + \theta_s$, with $\theta_f = \int_0^t \Omega(t')dt'$, allows the use of $\theta_s(t)$ for the slow evolution of the VLF wave.

The arguments within the trigonometric functions in equations (6-43) through (6-45) can be rewritten in terms of the longitudinal electron phase

$$\zeta = kz - \omega t \quad \int_0^t \Omega(t')dt', \tag{6-47}$$

where $\psi + \Theta = \psi + \theta_f + \theta_s = \zeta + \theta_s + \phi$. Defining the electron longitudinal phase velocity as

$$v = \dot{\zeta} = kv_z - \omega + \Omega_0\left(1 + \frac{qc^2 t^2}{n^2}\right), \tag{6-48}$$

where (6-46) is used to replace z in terms of t in the inhomogeneous term. Thus, the electron phase acceleration becomes

$$\ddot{\zeta} = \dot{v} = k\dot{v}_z + 4q\frac{\omega^3}{k^2}t. \tag{6-49}$$

79

Substituting the electron phase and electron phase velocity into equations (6-43) through (6-45) while using (6-46) for the macroscopic z terms, $v_{z_0} = \omega/k$ for the macroscopic terms, and $v_{z_0} = -c/n$ in the microscopic terms yields

$$\dot{v} = \left(4 - v_0^2\right)\frac{q\omega^3}{k^2}t + |b|v\omega\sin(\zeta + \theta + \phi), \qquad (6\text{-}50)$$

$$\dot{v} = \frac{vq\omega^2}{k^2}t + 2|b|\sin(\zeta + \theta + \phi), \qquad (6\text{-}51)$$

$$\dot{\theta} = \frac{2|b|}{v}\cos(\zeta + \theta + \phi), \qquad (6\text{-}52)$$

where the definition $v = kv_\perp$ is a normalized perpendicular velocity, $v_0 = kv_{\perp 0}$ is the normalized perpendicular velocity at the equator, and the subscript s is dropped from θ_s, since all coordinates are now slowly evolving. The macroscopic z motion along the inhomogeneous field line uses the substitution $z=ct/n$. The microscopic z describing electron bunching in the VLF wave uses the fact that the wave and electrons are counter-propagating which causes $v_{z0} = -c/n$.

The first term on the right side of equations (6-50) and (6-51) represents the acceleration of the hot electrons due to the inhomogeneity of the earth's magnetic field. The acceleration term is analogous to the "taper" term in a free electron laser as discussed in Chapter V, and so the acceleration term is referred to as a "taper" here. Define

$$\delta = \frac{\omega^2 q}{k^2} = \frac{9\omega^2}{2k^2L^2R_e^2}, \qquad (6\text{-}53)$$

where L defines the number of geocentric earth radii at the equator to the magnetic field line being used, and $R_e = 6370$ km is the mean radius of the

earth. Presenting the hot electron equations of motion using the taper term gives

$$\dot{v} = \left(4 - v_0^2\right)\delta\omega t + |b|v\omega \sin\left(\zeta + \theta + \phi\right) \tag{6-54}$$

$$\dot{v} = v\delta t + 2|b|\sin\left(\zeta + \theta + \phi\right) \tag{6-55}$$

$$\dot{\theta} = \frac{2|b|}{v}\cos\left(\zeta + \theta + \phi\right). \tag{6-56}$$

Several interesting observations can be made about the equations of motion (6-54) through (6-56). Equation (6-54) follows the longitudinal evolution of the electrons, and includes the pendulum equation with a phase acceleration identified as taper. The taper term in equation (6-54) shows that certain electrons with an equatorial normalized perpendicular velocity of $v_0 \pm 2$ experience no effect on their longitudinal phase velocity due to the inhomogeneity of the earth's magnetic field. A normalized perpendicular velocity of $v_0 = \pm 2$ corresponds to a pitch angle of $\approx \pm 63°$. The electron phase velocity, $v = kv_z(t) - \omega + \Omega(t)$, shows that the parallel velocity and the gyro-frequency are each changing in opposite directions at the same rate at this particular pitch angle, thereby canceling. The perpendicular velocity is only slightly affected by taper since (6-55) evolves much slower than the longitudinal phase velocity equation (6-46) due to the presence of the large factor $\omega \approx 10^4/s$.

C. NUMERICAL SIMULATIONS

The equations of motion (6-54) through (6-56), together with the wave equation (6-24), are now numerically integrated. The solutions reveal many of

the same characteristics found in free electron lasers, including the observation of electron-bunching, saturation, trapped particle instability, and taper.

The parameters used for the simulations are taken from measurements made by the Space, Telecommunications, and Radioscience Laboratory at Stanford University from Siple Station, Antarctica. This data was obtained using their >100 kW transmitter to send VLF signals at between one and six kilohertz using a long horizontal dipole antenna [26]. The amplified signals were then received at the conjugate point at Lake Mistissini, Quebec [26]. The data being simulated here is a transmitted signal at $\omega = 10^4$/s estimated by the observers through time of flight measurements as traveling along approximately the $L = 5$ field line. An index of refraction within the interaction region close to the equator was estimated to be approximately $n = 25$. The hot electrons present are represented by electrons uniformly spread in the electron phase, $\zeta_o = 0 \rightarrow 2\pi$, and the electron cyclotron phase, $\theta_o = 0 \rightarrow 2\pi$. The time of interaction is taken to be $T=1$s.

The first case examined is in the weak-field, high-gain regime. In an FEL, a weak optical field is identified by $|a| < \pi$. Similarly, a weak whistler field is identified when $|b|\omega T^2 \leq \pi$ which corresponds to $|b| \approx 3 \times 10^{-4}$/s [27]. Figure 6-3 shows the results of high gain in a weak whistler field of initial value $b_0 = |b(0)| = 5 \times 10^{-5}$/s as it interacts with a hot plasma of frequency of $\omega_h = 0.2$/s. The electron beam has a small Gaussian spread in phase velocities characterized by width standard deviation $\sigma_v = 0.5$ /s about the initial phase velocity $v_0 = 0$. All electrons have a normalized perpendicular velocity of $v_0 = 1$ corresponding to an initial pitch angle of $\pi/4$. The whistler's frequency is $\omega = 10^4$ /s with an interaction time of $T = 1$ second. The taper term is $\delta = 0$, which indicates a homogeneous magnetic field. An FEL, with current density

$i \geq \pi$ is in the high gain regime and experiences exponential gain. Similarly, when $\omega_h^2 \omega T^3 \geq \pi$, (or $\omega_h \geq \sqrt{\pi/\omega T^3} \approx 0.02/s$) the whistler wave is said to be in the high gain regime where exponential growth occurs [27]. After a characteristic time elapses allowing the electrons to bunch (approximately 0.35s in this example) the gain becomes exponential. In an FEL the exponential gain is calculated from $_{FEL}(\tau) \approx exp\left[(j/2)^{1/3}\sqrt{3}\tau\right]/9$ [1]. Similarly, the exponential gain for the whistler wave is calculated by [27]

$$G(T) \approx exp\left[\left(\omega\omega_h^2/2\right)^{1/3}\sqrt{3}T\right]/9. \qquad (6\text{-}57)$$

Equation (6-57) yields a final gain after the one second interaction of $G \approx 34$ dB. This value is slightly larger than that shown in Figure 6-3 since equation (6-57) does not take into account gain degradation due to a spread in electron longitudinal phase velocities or the delay due to the bunching time. The phase is shifted linearly by nearly the same factor used in the exponential to calculate the gain, $\Delta\phi \approx \left(\omega\omega_h^2/2\right)^{1/3}T/2 \approx 3$ [27]. The phase space in (ζ, v) displays the final positions of 2000 sample electrons after the one-second interaction. Those electrons going up in phase velocity remove energy from the wave, while the electrons going down in phase velocity transfer more energy to the wave and cause amplification. The bunching of electrons in phase is clearly present at two locations in phase space since there are two phase factors ($\zeta_0 = 0 \rightarrow 2\pi$ and $\theta_0 = 0 \rightarrow 2\pi$) within the trigonometric functions in the equations of motion. The two dark horizontal lines on the phase-space plot show the maximum height of the closed-orbit region given by $\Delta v_s \approx 4\sqrt{|b|\omega T^2}$ (see Figure 6-3).
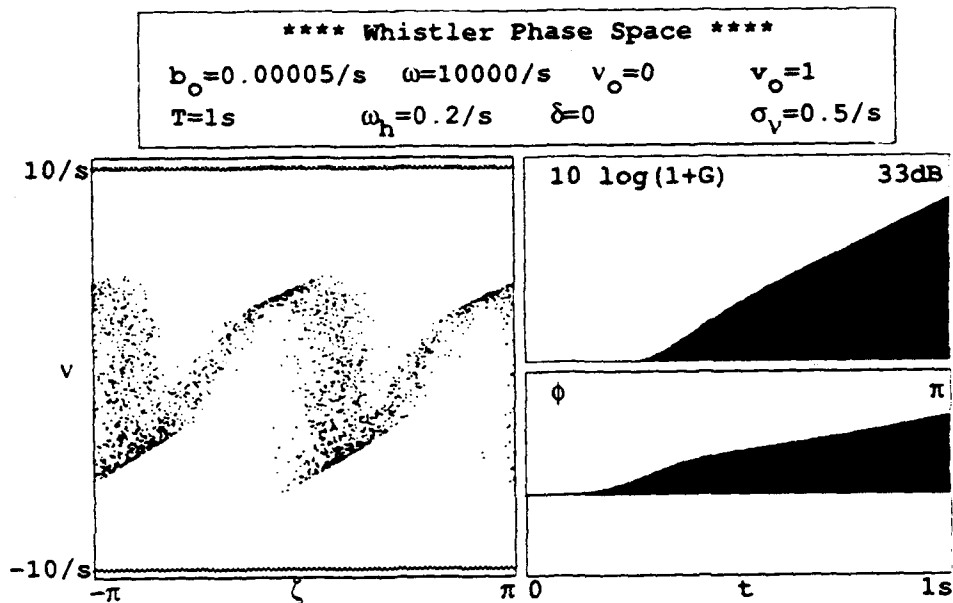
Figure 6-3. Whistler interaction in a weak VLF field with high gain.

Most whistlers reach strong field saturation during the interaction time. Once saturation occurs the electrons become trapped in closed orbits in phase space and execute synchrotron oscillations at a frequency $\omega_s \approx \sqrt{\omega|b|}$ [27]. These oscillations can evidence themselves as oscillations in the power and gain of the whistler wave. Figure 6-4 shows the results of a Gaussian distribution of hot electrons of width $\sigma_v = 10$ /s about the resonant phase velocity $v_0 = 0$ interacting with a strong whistler field for a time of T = 0.4 s. The electrons are at a pitch angle of $\pi/4$ determined by v_0=1.0, with a density corresponding to a hot plasma frequency of $\omega_h = 10$/s. The whistler wave has an initial amplitude $b_0 = |b(0)|$=0.01/s with frequency $\omega = 10^4$ /s . Again, there is no taper so $\delta = 0$. The phase space plot of Figure 6-4 shows the final positions of 3000 sample electrons showing their bunching at two phase regions and each with lower energy. The spread in phase velocities causes the bunching to be

more diffuse and creates much of the random scatter of electrons seen in the phase-space plot. Electrons appearing outside the final separatrix lines have been trapped by the previously larger whistler field in the oscillating pattern seen in the gain plot. Note that the final gain is at a minimum caused by the synchrotron oscillations.


```
**** Whistler Phase Space ****
b_o=0.01/s   ω=10000/s   v_o=0        V_o=1
T=0.4s       ω_h=10/s    δ=0          σ_v=10/s
```
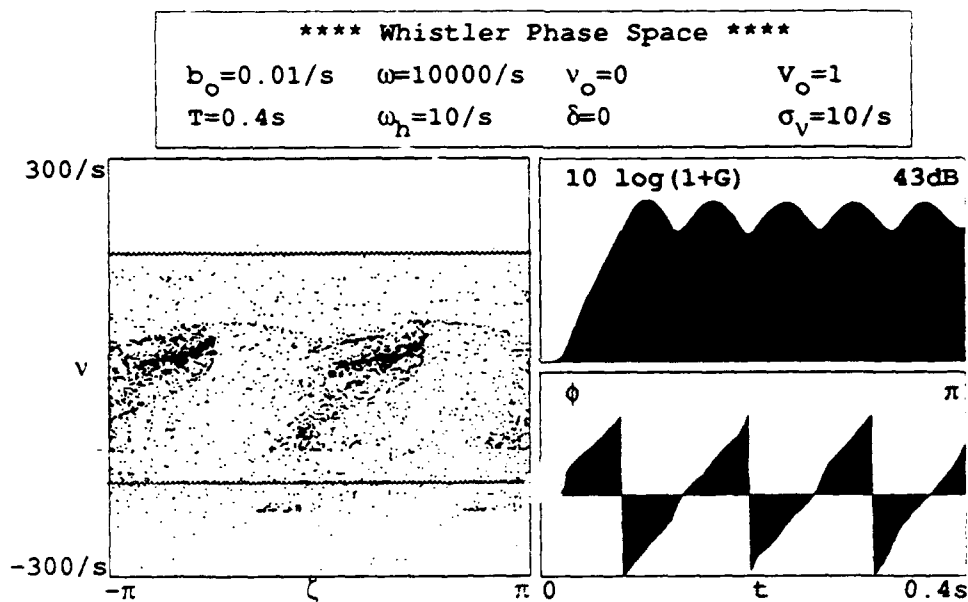
Figure 6-4. Whistler interaction in a strong VLF field with high gain.

The beginning of the gain curve shows that after the short bunching time, the gain is exponential until strong field saturation occurs at a value of $|b|_s \approx 2\left(\omega_h^4/4\omega\right)^{1/3} \approx 1.3$ /s. The strong fields trap the electrons and cause them to perform synchrotron oscillations. The presence of approximately 4.5 synchrotron oscillations is clear in the gain plot and agrees closely with the calculated value of $\omega_s \approx \sqrt{\omega|b|} \approx 36\pi$ /s which would predict 7 full oscillations

over the interaction time of 0.4s. The small discrepancy between the number of synchrotron oscillations observed and the estimate $\omega_s \approx 36\pi$ /s occurs because of the spread in electron phase velocities. Saturation in strong fields, electron trapping and synchrotron oscillations are all nonlinear effects observed in both FELs and whistler waves [27].

The previous figures used a short time of interaction and a homogeneous magnetic field with $\delta = 0$. For a longer interaction time, the effects of the inhomogeneity in the earth's magnetic field acts as a phase acceleration analogous to taper in an FEL. In Figure 6-5, the electrons begin away from the geomagnetic equator and far off resonance with a Gaussian spread of phase velocities characterized by a width $\sigma_v = 10$ /s centered at $v_0 = 2360$ /s. The electrons have an equatorial pitch angle of $\pi/4$ determined by $v_0 = 1$, with a density creating a hot plasma frequency of $\omega_h = 10$ /s. These hot electrons interacting with an initially weak whistler field of $b_0 = |b(0)| = 0.01$ /s of frequency $\omega = 10^4$ /s for a time of T = 1 s. The taper value of $\delta = 0.2\pi$ corresponding to the duct at $L \approx 5$ with index of refraction $n \approx 25$. The phase-space diagram displays the final positions of 3000 sample electrons. The electrons begin far above resonance, but their phase velocity decreases as they move into resonance near the geomagnetic equator. The simulation is designed so the sampled electrons are in resonance with the wave at the geomagnetic equator at a time $t = T/2$. After strong coupling between the hot electrons and the VLF wave near the equator, the taper causes the electrons to increase their phase velocity as they move past the equator and away from resonance. However, as seen in Figure 6-5 most of the electrons are trapped by the strong whistler wave field and continue to give energy to the wave.
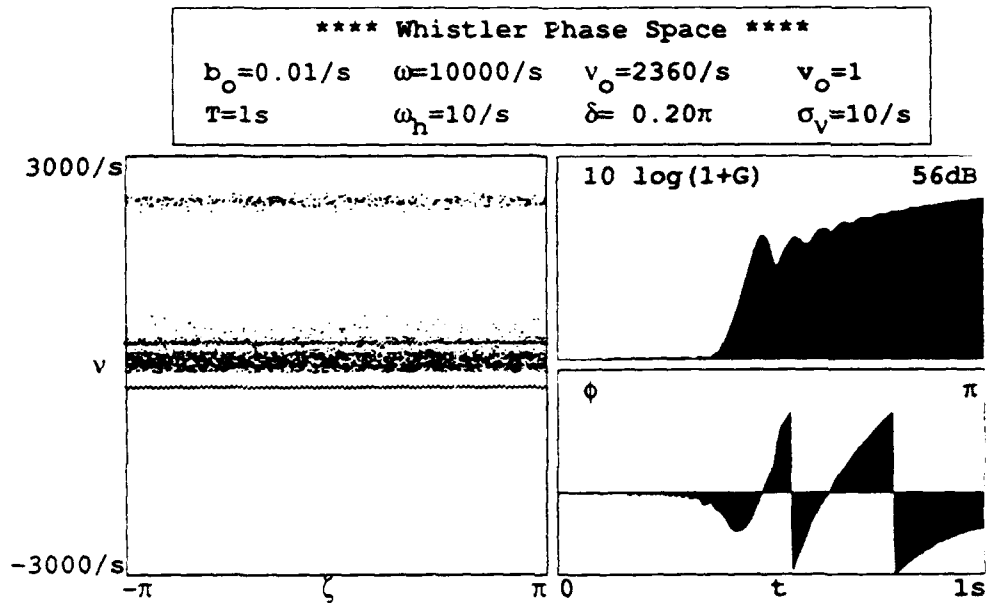
Figure 6-5. Whistler interaction in a inhomogeneous magnetic field with a strong VLF field and high gain.

The gain evolution in this figure shows no coupling between the electrons and whistler until the electrons' phase velocity is nearly resonant at time $t = 0.5$ s. Once sufficiently near resonance, the electrons become bunched and the gain becomes exponential. Synchrotron oscillations begin. The effect of the taper causes the trapped electrons to continue to give up energy to the wave after the normal saturation. Most of the electrons remain trapped near resonance by the strong whistler field, even though the earth's dipole field provides a phase acceleration to move them away from resonance. Those electrons not trapped by the strong VLF wave are moved off resonance by the taper. The gain evolution shows that because the electrons are far off resonance initially, there is no growth in the wave. As the electrons approach resonance at the equator, the same exponential growth seen in the homogeneous case occurs in the wave,

87

leading to saturation and synchrotron oscillations. The inhomogeneity of the earth's magnetic field provides a phase acceleration that allows continued energy extraction from the trapped electrons. This is seen as the gain slowly increases even after the homogeneous saturation level. The wave's phase initially decreases, a characteristic of tapering, and then begins to grow quickly. The rate of phase growth decreases in conjunction with decreasing gain growth. The general characteristics of the gain and phase evolutions shown in Figure 6-5 are in agreement with those obtained by Carlson et. al. of Stanford University [28]. Their simulations also show gain initially growing exponentially and then reaching either a steady value or growing slowly [28]. They also found the phase would initially decrease during the exponential growth, and then would increase parabolically [28].

D. CONCLUSIONS AND FURTHER RESEARCH SUGGESTIONS

Although apparently an unrelated process, the amplification of whistler waves is shown in this chapter to be closely related to the amplification of an optical wave in a free electron laser. The radiation field in both whistlers and FELs couples in resonance to "wiggling" electrons for efficient energy transfer. Nonlinear effects such as saturation and the trapped-particle instability are observed in both. For the whistler, the inhomogeneity of the earth's magnetic field lines acts in an analogous manner to tapering an undulator. The electron equations of motion and the wave equation derived in the chapter are used show many of the same effects seen in whistler and FEL research. The results closely reproduce the results of other researchers using more traditional approaches to the study of whistler wave amplification.

This chapter solves for whistler wave amplification of a single mode using either monoenergetic hot electrons or electrons in a Gaussian distribution of phase velocities with a single pitch angle. Further, all electrons are forced to be in resonance at the equator, or at time $t = T/2$, regardless of their initial phase velocity. The research needs to be extended by adding a more realistic distribution of hot electron energies and pitch angles. A multimode numerical simulation should be developed, similar to those used in FEL research, so that the experimentally observed sweeps in frequency of the whistler waves can be investigated numerically.

LIST OF REFERENCES

[1] W.B. Colson, Chapt.5 in: *Free Electron Laser Handbook*, ed. W.B. Colson, C. Pellegrini, and A. Renieri, North Holland Publishers, 1989.

[2] J.M.J. Madey, J. Appl. Phys. **42,** 1971, 1906.

[3] H. Motz, J. Appl. Phys. **22,** 1951, 527.

[4] R.M. Phillips, IRE Trans. Electron Devices **7,** 1960, 231.

[5] L.R. Elias, W.M. Fairbanks, J.M.J. Madey, H.A. Schwettman, T.I. Smith, Phys. Rev. Lett. **36,** 1976, 717.

[6] D.A.G. Deacon, L.R. Elias, J.M.J. Madey, G.J. Ramian, H.A. Schwettman, and T.I. Smith, Phys. Rev. Lett. **38,** 1977, 892.

[7] W.B. Colson, Phys. Lett. **64A,** 1977, 190.

[8] W. B. Colson and J. L. Richardson, "Multimode Theory of Free Electron Laser Oscillators", Phys. Rev. Lett. **50** 1983, 1050.

[9] W.B. Colson, in: *Free Electron Lasers: Critical Review of Technology*, ed. B.E. Newnam, Proc. SPIE **738** 1988.

[10] J.D. Jackson, chapt.14 in: *Classical Electrodynamics*, John Wiley Publishers, 2d ed. 1975.

[11] W.B. Colson, Nucl. Instr. & Methods in Phys. Res. **A296,** 1990 348-350.

[12] G. Dattoli, Chapt.7 in: "Free Electron Laser Handbook", ed. W.B. Colson, C. Pellegrini, and A. Renieri, North Holland Publishers, 1989.

[13] P. Elleaume, IEEE J. Quantum Electron. **QE-21,** 1985, 1012-1022.

[14] G. Dattoli, A. Renieri, A. Torre, J. Gallardo, Phys. Rev. **A35,** 1987, 4175-4180.

[15] G. Dattoli, T. Hermsen, L. Mezi, A.Torre, J.C. Gallardo, Nucl. Instrum. Methods, **A272,** 1988, 351-363.

[16] G. Dattoli, T. Hermsen, A. Renieri , A.Torre, J.C. Gallardo, Phys. Rev. **A37**, 1988, 4326-4333.

[17] G. Dattoli, T. Hermsen, A. Renieri , L. Mezi, A.Torre, J.C. Gallardo, Phys. Rev. **A37**, 1988, 4134-4139.

[18] E. Zauderer, *Partial Differential Equations of Applied Mathematics,* 2nd ed., John Wiley and Sons, New York, 1989, pp 48-54.

[19] D.C. Quimby, C.G. Parazzoli, J.B. Romero, B.D. McVey, and D.A. Byrd, Nucl. Inst. and Meth. **A318** 1992 680-690.

[20] D.C. Quimby, C.G. Parazzoli, and D.J. Pistoresi, Nucl. Inst. and Meth. **A318** 1992, 628-635.

[21] L.R.O. Storey, " An investigation of Whistling Atmospheres", Philosophical Transactions of the Royal Society of London, **246**, 1953, 113-141.

[22] R.A. Helliwell, *Whistlers and Related Phenomena,* Stanford University Press, 1965.

[23] U. Inan, "Non-linear Gyroresonant Interaction of Energetic Particles and Coherent VLF Waves in the Magnetosphere", PhD Dissertation, Stanford University, California, 1977.

[24] F.F. Chen, *Plasma Physics and Controlled Fusion, Volume 1: Plasma Physics,* 2d ed., Plenum Press, 1990.

[25] U.S. Inan, R.A. Helliwell, W.S. Kurth, "Terrestrial Versus Jovian VLF Chorus; A Comparative Study", Journ. of Geophys. Res., **88**, 1983, 6171-6180.

[26] R.A. Helliwell, "VLF Wave Stimulation Experiments in the Magnetosphere from Siple Station, Antarctica", Reviews of Geophysics, **26**, no.3, 1988, 551-578.

[27] W. B. Colson, B. Gately, D. L. Caudle, and K. A. Sturgess, "Analogies Between the Free Electron Laser and Whistler Mode Amplification in the Magnetosphere", presented at the 14th International Free Electron Laser Conference in Kobe, Japan, August 21, 1992.

[28] C.R. Carlson, R.A. Helliwell, and U.S. Inan, "Space-Time Evolution of Whistler Mode Wave Growth in the Magnetosphere", 1990, 15073-15089.

INITIAL DISTRIBUTION LIST

1. Defense Technical Information Center   2
    Cameron Station
    Alexandria, Virginia 22304-6145

2. Library, Code 52   2
    Naval Postgraduate School
    Monterey, California 93943-5002

3. Professor William B. Colson, Code PH/Cw   6
    Department of Physics
    Naval Postgraduate School
    Monterey, California 93943-5000

4. Professor K. E. Woehler, Code PH/Wh   1
    Chairman, Department of Physics
    Naval Postgraduate School
    Monterey, California 93943-5000

5. Professor John Neighbours, Code PH/Nb   1
    Department of Physics
    Naval Postgraduate School
    Monterey, California 93943-5000

6. Professor Robert Armstead, Code PH/Ar   1
    Department of Physics
    Naval Postgraduate School
    Monterey, California 93943-5000

7   Professor Rudulf Panholzer, Code SS/Pz   1
    Department of Space Science
    Naval Postgraduate School
    Monterey, California 93943-5000

8. Professor Maurice Weir, Code MA/We   1
   Department of Mathematics
   Naval Postgraduate School
   Monterey, California 93943-5000